Hefny *et al. Swiss J Geosci (2020) 113:11*
https://doi.org/10.1186/s00015-020-00364-4

SGG SGS sc | nat
Swiss Journal of Geosciences

ORIGINAL PAPER Open Access

A laboratory approach for the calibration of seismic data in the western part of the Swiss Molasse Basin: the case history of well Humilly-2 (France) in the Geneva area

Mahmoud Hefny[1,2*], Alba Zappone[3,4*], Yasin Makhloufi[5], Antoine de Haller[5] and Andrea Moscariello[5]

Abstract

A collection of 81 plugs were obtained from the Humilly-2 borehole (France), that reached the Permo-Carboniferous sediments at a depth of 3051 m. Experimental measurements of physical parameters and mineralogical analysis were performed to explore the links between sedimentary facies and seismic characteristics and provide a key tool in the interpretation of seismic field data in terms of geological formations. The plugs, cylinders of 22.5 mm in diameter and ~30 mm in length were collected parallel and perpendicular to the bedding in order to explore their anisotropy. Ultrasound wave propagation was measured at increasing confining pressure conditions up to 260 MPa, a pressure where all micro-fractures are considered closed. The derivatives of velocities with pressure were established, allowing the simulation of lithological transitions at in-situ conditions. At room conditions, measured grain densities (kg/m^3) range from 2630 to 2948 and velocities vary from 4339 to 6771 and 2460 to 3975 m/s for P- and S-waves propagation modes, respectively. The largest seismic-reflections coefficients were calculated for the interface between the evaporitic facies of the Keuper (Lettenkohle) and the underlying Muschelkalk carbonates ($R_C = 0.3$). The effective porosity has the range of 0.23% to 16.65%, while the maximum fluid permeability (m^2) is 9.1×10^{-16}. A positive correlation between porosity and ultrasound velocity has been observed for P- and S-waves. The link between velocities and modal content of quartz, dolomite, calcite, and micas has been explored. This paper presents a unique set of seismic parameters potentially useful for the calibration of seismic data in the Geneva Molasse Basin.

Keywords: Ultrasound seismic velocities, Geothermy, Borehole rock samples, Reflectivity, Swiss Molasse

1 Introduction

Seismic reflection imaging is a fundamental tool for evaluating the geometry of the deep reflectors within the Earth's crust (Brown 1986; Claerbout 1985; Schilt et al. 1979). Nevertheless, seismic velocity distribution at depth cannot be resolved only with the aid of seismic reflection methods and other independent geophysical methods need to be applied. Furthermore, if the formations that compose the geological section under scrutiny have a similar mineralogical composition and/or if bedding and layering are not pronounced, imaging the geological sequence by using the reflection seismic method can be quite problematic. One possibility to help understanding the origin of seismic reflectors is to use the laboratory experiments at ultrasonic frequency and under high-confining pressure, which simulate in-situ subsurface conditions. This method has been successfully applied in numerous studies and in different

Editorial handling: Wilfried Winkler.

*Correspondence: mhefny@ethz.ch; alba.zappone@sed.ethz.ch
[2] Geology Department, South Valley University, Qena 83523, Egypt
[4] Department of Mechanical and Process Engineering, ETH Zürich, 8092 Zürich, Switzerland
Full list of author information is available at the end of the article

(See figure on next page.)

Fig. 1 Geological map and structural framework of the western Swiss Molasse Basin (modified after Clerc et al. 2015; Makhloufi et al. 2018). The seismic profile AB (located on the map) crosses the Geneva Basin and intersects the Humilly-2 well location; it shows the main stratigraphic units. The geological units have been produced by time-to-depth conversion using the available seismic transect and the seismic velocity derived from the sonic log of Humilly-2 borehole (after Gorin et al. 1993; Moscariello 2016)

environments (e.g. Almqvist et al. 2013; Barberini et al. 2007; Birch 1960; Wenning et al. 2016; Zappone et al. 2000). In the present work we apply this approach for the geological interpretation of the seismic data recorded in the Southwestern part of the Swiss Molasse Basin.

The Geneva Basin (GB), in the westernmost part of Swiss Molasse Basin, has been the object of intense seismic reflection exploration for hydrocarbon (Gorin et al. 1993). Between 1958 and 1990, about 300 km of deep reflection seismic have been acquired, and a 16 km long, composite seismic transect was presented (Gorin et al. 1993; Moscariello 2016). Following the unsuccessful hydrocarbon exploration campaigns, interest in the GB has been renewed by geothermal investigations. A geothermal exploration program in Canton Geneva aims at producing geothermal energy from hot water in Mesozoic sediments (Moscariello 2019). In order to do that, the project has to evaluate the potential reservoirs through the integration of available geological and geophysical data. It focuses on the area stretching from the folded Jura Mountains in the north to the Mount Salève ridge in the south (Moscariello 2016).

More recently a transnational French-Swiss project within the European project GeoMol (2014–2021) developed new studies over an area of 2800 km^2 in the Savoy-Geneva region, and used 985 km of available 2D seismic dataset (800 km over French territory, and 185 km over the Swiss territory) together with logs of 43 available deep boreholes loggings (including bottom hole temperature; BHT) to reconstruct a 3D geological model and temperature distribution model for the sedimentary basin. Available logs from the wells Humilly-2 and Thônex-1 were used to calibrate stratigraphic boundaries with seismic horizons in the GB (Fig. 1). Thônex-1 is a deviated, geothermal exploration well drilled in 1993. It reached a total depth of 2530 m in marly Jurassic limestones (Jenny et al. 1995). The vertical Humilly-2 (HU2) borehole is the deepest well drilled in the GB during a 1960s hydrocarbon exploration campaign in nearby France. Among all boreholes penetrating the entire Mesozoic succession in the area, HU2 is the only one where several stratigraphic intervals were cored down to a total depth of 3051 m in the top of the Permo-Carboniferous (Fig. 1; Marti 1969). HU2 (46° 6′ 53″ N and 6° 1′ 30″ E) is located on the composite seismic profile shown in Fig. 1 (see also Sommaruga et al. 2012). Well logs, including gamma ray and sonic, were run over the entire section penetrated in HU2 (Fig. 2) and used to tie with the seismic data.

Six regional reflectors are commonly interpreted in the GB (Gorin et al. 1993; Clerc et al. 2015; Rusillon 2018). From top to bottom, they are: top Urgonian (base Tertiary), top argillaceous Upper Jurassic, top Middle Jurassic, top Lower Jurassic, top evaporitic Triassic and top carbonate Triassic (Fig. 2). The basal Triassic unit of the Buntsandstein is too thin to be seismically interpreted. HU2 reached total depth in Permo-Carboniferous sandstones characterized by a transparent seismic facies. The latter sequence is often underlain by an interval of high-amplitude negative reflections interpreted as coal-bearing Permo-Carboniferous sediments (Gorin et al. 1993). Where this reflective sequence comes close to the Triassic, it highlights the angular unconformity between Triassic and Permo-Carboniferous sediments (Signer and Gorin 1995).

This paper summarizes the results of elastic wave velocity measurements combined with both thin section observations in optical microscopy and quantitative micro-textural analysis using the automated QEMSCAN technique, carried out on core samples from HU2. The purpose of this paper is to quantify the effect of porosity, mineral composition and micro-textural characteristics, such as banding and layering of minerals, of sedimentary rocks on seismic properties. The final aims of this paper are twofold: (1) to provide a potential contribution to the interpretation of seismic reflectivity zones in a 3D seismic survey to be acquired for geothermal exploration in the GB; (2) to investigate the possible use of these measurements in the calibration of borehole logs when cores are missing.

2 Geological and tectonic setting

2.1 Regional geology

The Molasse Basin (MB) is located at the northern front of the Alps. It stretches from France (Savoy) through Switzerland up to southern Germany (Bavarian foreland) with a regional WSW-ENE trend and connects in Austria with the Vienna and Pannonian Basins (Fig. 1). The MB is a Cenozoic foreland basin which formed as a response to flexural subsidence during the collision of Eurasia and Adriatic-Africa plates (Pfiffner 1986; Véron 2005). Its substratum comprises Mesozoic (locally Permo-Carboniferous) sediments and crystalline metamorphic

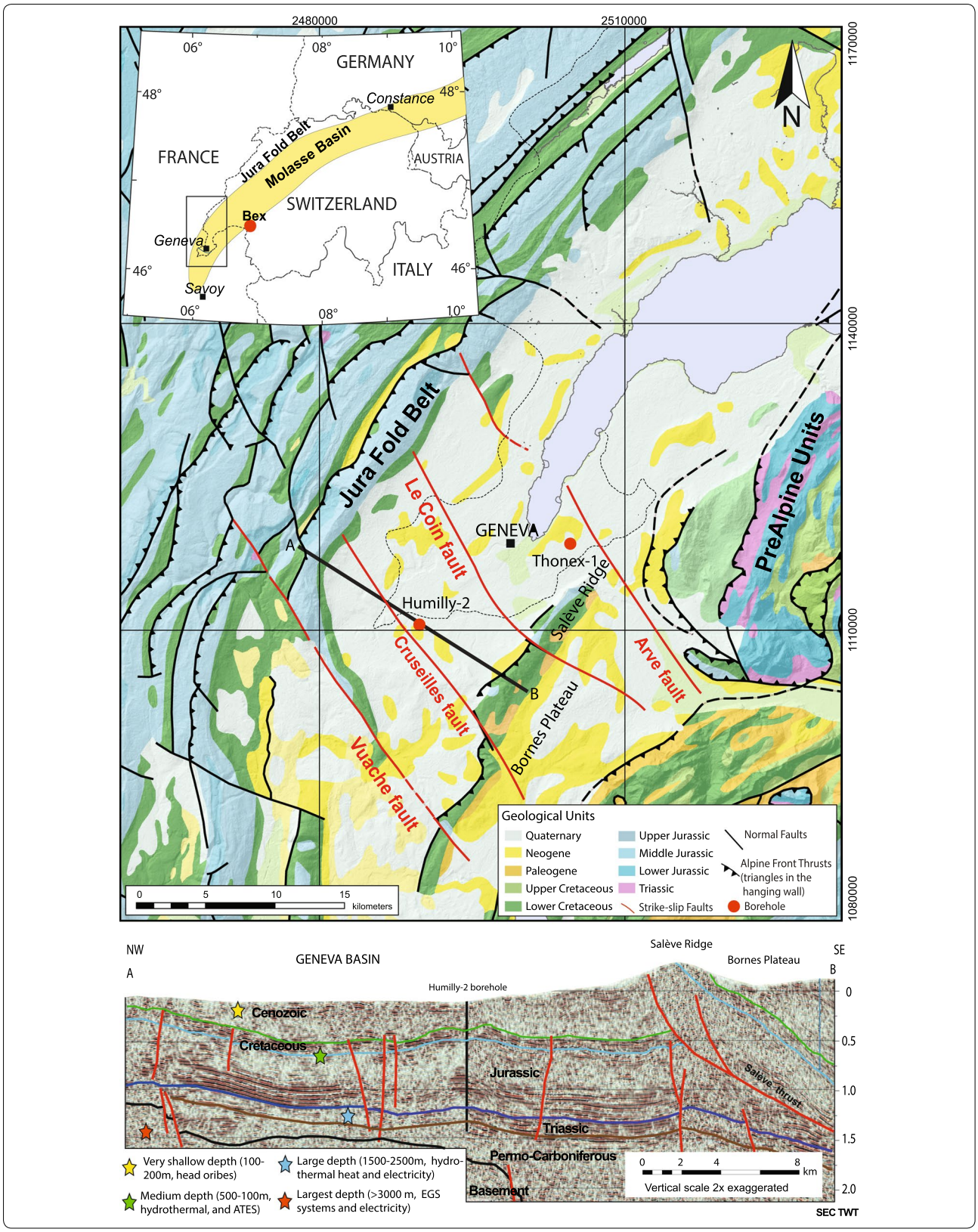
2480000
2510000
1170000
1140000
1110000
1080000
GERMANY
FRANCE
AUSTRIA
SWITZERLAND
ITALY
Constance
Jura Fold Belt
Molasse Basin
Bex
Geneva
Savoy
N
Jura Fold Belt
Le Coin fault
GENEVA
Thonex-1
Humilly-2
Salève Ridge
Arve fault
Cruseilles fault
Bornes Plateau
Vuache fault
PreAlpine Units
A
B
Geological Units
Quaternary
Neogene
Paleogene
Upper Cretaceous
Lower Cretaceous
Upper Jurassic
Middle Jurassic
Lower Jurassic
Triassic
Strike-slip Faults
Normal Faults
Alpine Front Thrusts (triangles in the hanging wall)
Borehole
0 5 10 15 kilometers
NW
A
GENEVA BASIN
Salève Ridge
Bornes Plateau
SE
B
Humilly-2 borehole
Cenozoic
Cretaceous
Jurassic
Triassic
Permo-Carboniferous
Basement
Salève thrust
0 2 4 8 km
Vertical scale 2x exaggerated
0
0.5
1.0
1.5
2.0
SEC TWT
Very shallow depth (100-200m, head oribes)
Medium depth (500-100m, hydrothermal, and ATES)
Large depth (1500-2500m, hydro-thermal heat and electricity)
Largest depth (>3000 m, EGS systems and electricity)

basement rocks. The MB is divided into two geomorphological entities; the deformed and undeformed sub-units. The undeformed "platform" Molasse comprises 90% of the basin, while the folded and deformed "subalpine" Molasse is located along the southernmost flank of the basin (Véron 2005).

The Swiss Molasse Basin (SMB) occupies the western and central part of the MB, stretching over approximately 300 km between Savoy in the SW (30 km wide) and Lake Constance in the NE, where it reaches a width of 80 km. The Savoy-Geneva area is located at the southwesternmost end of the SMB. It is the result of a geological evolution initiated in the Palaeozoic (Schegg et al. 1999, and references therein), forming a narrow (max. 40 km in width) elongated (~110 km in length) NNE-SSW depression. This depression is limited to the northwest by the Jura fold belt, to the southeast by the thrusted anticlinal ridge of the Salève and to the west by the Vuache anticline. The Salève ridge is intersected by several NW-SE trending sinistral wrench faults, which acted as transfer faults during thrust tectonics and influenced the distribution of the Tertiary deposition within SMB (Fig. 1).

2.2 Swiss Molasse Basin evolution

The present-day configuration of the SMB and its substratum underwent four major tectonic events (Schegg et al. 1999, and references therein): (a) Variscan orogeny and the subsequent formation of a series of narrow, deep, SWS–ENE and WNW–ESE trending Permo-Carboniferous grabens, filled by clastic sediments (Thury et al. 1994; (b) extension related to the sag-basin development and thermal subsidence during the Mesozoic (Loup 1992; (c) closure of Late Cretaceous Alpine flysch basins and development of the North Alpine Foreland Basin as a flexural depression during the late Cretaceous-early Miocene (Lihou and Allen 1996; (d) detachment of Mesozoic and Cenozoic sediments on Triassic evaporites, deformation and uplift/inversion during the Miocene to Pliocene (Schegg and Leu 1996).

The tectonic elements responsible for the Geneva basin structuration are controlled by four major NW–SE trending wrench-fault systems. Their continuations across the Geneva Basin were revealed on the 2D seismic data and link the subalpine units with the Jura Mountains across the Bornes Plateau, the Salève ridge and the Geneva Basin (Clerc et al. 2015, and references therein). Detailed information of the basin evolution, and about the depositional environments are described in Brentini (2018).

2.3 Stratigraphy of the GB

The stratigraphy of GB consists of a 3–5 km thick sequence of Mesozoic and Cenozoic sedimentary rocks overlying Permo-Carboniferous sediments and Variscan crystalline basement. The Mesozoic and Cenozoic sequence dips gently (1°–3°) southeastwards towards the Alpine foreland (Fig. 2). A detailed study of the stratigraphic framework at basin-scale is presented in Brentini (2018).

The basement is mainly composed of biotite-rich gneiss, green schist and porphyritic granite resulting from the Palaeozoic Variscan orogeny (Matte 2001). Permo-Carboniferous siliciclastic sediments are locally present above this basement. They represent the infill of several SW–NE narrow Palaeozoic (mostly Hercynian) extensional basins developed in the crystalline basement (Wilson et al. 2004; McCann et al. 2006). They present a large variation in lateral thickness, depending on the location and depth of the troughs. The lithology consists of tight brownish conglomerates and arkosic sandstones, interlayered with silty, and organic-rich clays deposited mainly in a lacustrine environment in association with fluvial deposits resulting from the erosion of the crystalline basement. The Mesozoic succession represent the thickest part of the sediments. Generally, in the SMB the main lithologies (limestones and marls, except for the Triassic) are correlated to the Helvetic domain, which corresponds to the distal part of the European margin at the time of deposition. However, the GB shows proximal facies, which are associated with the Jura domain. The top of the basement is characterized by an angular unconformity on which Mesozoic sediments were deposited (Signer and Gorin 1995; Sommaruga et al. 2017).

The Triassic is characterized by a marine transgression leading to the deposition of thick evaporitic series in an epicontinental sea environment (Disler 1914). The Buntsandstein (Lower Triassic) is mainly composed of sandstone. Conglomeratic and silty layers are intercalated in this formation (c.a 15 m in thickness in HU2). It is overlain by the Muchelkalk (Middle Triassic), composed of marly limestones, anhydrites and dolomites and the Keuper (Upper Triassic) formed by a thick evaporite deposits (gypsum/anhydrite and salt). Given the ductility of salt, the Keuper constitute the basal décollement for the foreland thrust system (Diepolder et al. 2015) and generates

(See figure on next page.)

Fig. 2 Stratigraphic column of well Humilly-2 with location of the potential reservoirs investigated. Location of investigated samples HU taken from cores and position of the six interpreted regional seismic reflectors. Cores were extracted in four depth intervals (I, II, III, and V in column "Core"). The depth interval IV is partially represented by samples from literature while the depth interval V corresponds to 3 sub-intervals: Permo-Carboniferous (VII), Lower Triassic (VI), and Middle Triassic (V) (see text for explanations). *Anis.* Anisian, *Hauteriv.* Hauterivian, *A.* Aleian, *Batho.* Bathonian, *Muschelk.* Muschelkalk

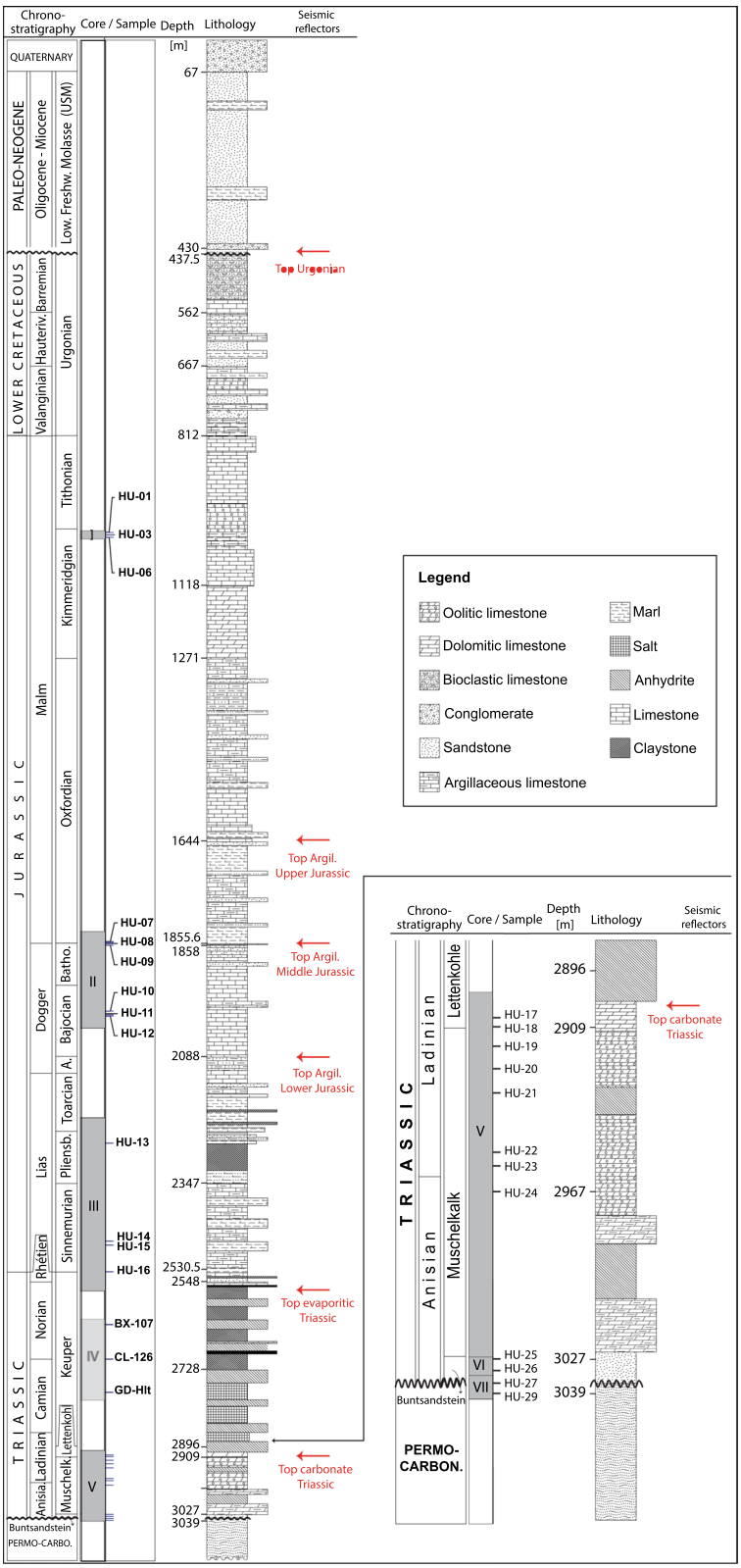
Chrono-stratigraphy
Core / Sample
Depth [m]
Lithology
Seismic reflectors
QUATERNARY
PALEO-NEOGENE
Oligocene - Miocene
Low. Freshw. Molasse (USM)
LOWER CRETACEOUS
Barremian
Hauteriv.
Valanginian
Urgonian
JURASSIC
Malm
Tithonian
Kimmeridgian
Oxfordian
Dogger
Batho.
Bajocian
A.
Lias
Toarcian
Pliensb.
Rhétien
Sinnemurian
TRIASSIC
Norian
Keuper
Camian
Ladinian
Lettenkohl
Muschelk.
Anisia
Buntsandstein
PERMO-CARBO.
HU-01
HU-03
HU-06
HU-07
HU-08
HU-09
HU-10
HU-11
HU-12
HU-13
HU-14
HU-15
HU-16
BX-107
CL-126
GD-Hlt
I
II
III
IV
V
67
430
437.5
562
667
812
1118
1271
1644
1855.6
1858
2088
2347
2530.5
2548
2728
2896
2909
3027
3039
Top Urgonian
Top Argil. Upper Jurassic
Top Argil. Middle Jurassic
Top Argil. Lower Jurassic
Top evaporitic Triassic
Top carbonate Triassic
Legend
Oolitic limestone
Dolomitic limestone
Bioclastic limestone
Conglomerate
Sandstone
Argillaceous limestone
Marl
Salt
Anhydrite
Limestone
Claystone
Chrono-stratigraphy
Core / Sample
Depth [m]
Lithology
Seismic reflectors
TRIASSIC
Ladinian
Anisian
Lettenkohle
Muschelkalk
Buntsandstein
PERMO-CARBON.
HU-17
HU-18
HU-19
HU-20
HU-21
HU-22
HU-23
HU-24
HU-25
HU-26
HU-27
HU-29
V
VI
VII
2896
2909
2967
3027
3039
Top carbonate Triassic

thrusts and duplexes, which produce large lateral variations in thickness (240 to 350 m; Brentini 2018).

The transgressive trend is still present during the Lower Jurassic leading to the deposition of limestones overlain by marls (Signer and Gorin 1995). The Middle Jurassic succession is characterized by a first regressive trend and a shift towards shallower conditions during the Bajocian and Bathonian (Strasser 1994). A second regressive trend affects the Upper Jurassic which exhibits the development of a shallow carbonate platform, extending towards the northwest. During the Kimmeridgian, existing structural highs saw the growth of patch-reefs (Meyer 2000; Makhloufi et al. 2018) while the sealing of inter-reef depressions by tidal deposits occurred during the Tithonian (Strasser 1994).

The Early Cretaceous saw shallow and warm-water conditions prevailing (Debelmas et al. 1961; Charollais et al. 2013) with low amplitude sea-level changes inducing several episodes of emersion and drowing characterized by the deposition of bioclastic limestones, bioturbated limestones and organic-rich marls. The Lower Cretaceous deposits are not recorded in the GB due to their emersion and later erosion during the early Cenozoic (Eocene-Oligocene). This event led to large-scale karstification of the Urgonian limestones. These karsts were later filled with Eocene lateritic sediments (Becker et al. 2013) and reworked Aptian-Albian Sediments. The Early Cretaceous limestones and Eocene lateritic sediments are overlain by alternations of continental sandstones and marlstones composing the Lower Freshwater Molasse. Both the Upper Marine and Upper Freshwater Molasse units are not preserved in the GB resulting from either the uplift of the Jura during the Miocene-Pliocene and/or by the glacial advances of the Pleistocene (Signer and Gorin 1995; Schegg and Leu 1996; Charollais et al. 2007).

3 Methods

Twenty-three samples from the five aquifers have been recovered from HU2 borehole; multiple cylindrical plugs with 25.4 mm diameter and 29.9–52.4 mm length were cut from the samples. Fig. 2 shows the position of the samples within the stratigraphic succession. Plugs were cut parallel and perpendicular to bedding in order to study the anisotropy of the elastic properties in each rock type. Because at Humilly the layering is sub-horizontal and the borehole is not deviated, the direction perpendicular to bedding (Z) coincides with the drilling axis. One or two mutually perpendicular plugs (X and Y directions) were cut in the bedding plane (Fig. 3). In addition, two plugs were cored at the depth of 107.35–108.5 m from an anhydrite rich interval of the BEX borehole, Bohrung-3 (Canton Vaud). A lathe machine was used to guarantee planar and parallel surfaces at the ends of the cylindrical plugs, with ±5 μm precision. The plugs were dried in an oven at 70 °C for 24 h to remove free water in pores and fractures, and stored in a desiccator, before performing further measurements.

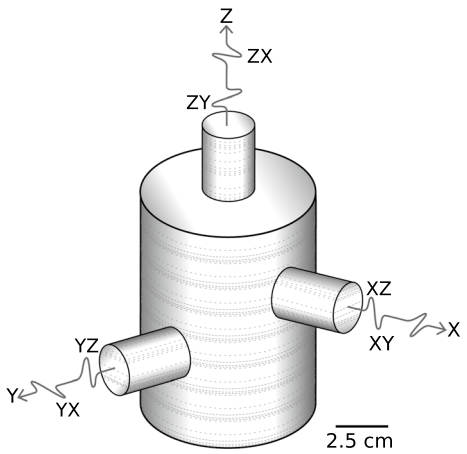

Fig. 3 Orientation of the plugs relative to bedding and to borehole core. The arrows show the propagation direction of the seismic waves. Therefore V_p(X), V_p(Y) and V_p(Z) correspond to the velocities of compressional waves along X, Y and Z directions, respectively. For shear waves, we used the following convention: the two letters identify the polarization plane while the direction of propagation is indicated by the second letter. For example, V_s(XZ) is the velocity of a shear wave polarized in the XZ plane and traveling in the Z direction

3.1 Compositional and mineralogical characterization

Thin sections for optical microscopy were prepared from the heads of the cylinders. In order to distinguish calcite from dolomite in carbonate samples, thin sections were stained using a proportional mixture of Alizarin Red S and Potassium Ferricyanide, using the adapted methodology of Dickson (1965). All thin sections were examined and photographed under an optical microscope using a camera Nikon DS-Fi2 on a Nikon Eclipse E600 Polarizing Light Microscope (POL) equipped with a NIS Element D software package.

Optical microscopy analysis was complemented by scanning electron microscopy analysis performed on thin sections at the University of Geneva (QEMSCAN QUANTA 650F), that provided high-resolution mineralogical maps and automated quantitative mineralogical compositions identification. Mineral identification was based on the combination of back-scattered electron values, energy-dispersive X-ray spectra, and X-ray count rates. Scanning was performed at 15 kV with a resolution of 7.5 μm on a 1 × 1 cm area. All these tools were integrated to assess the mineralogical composition, rock type, and vertical facies distribution.

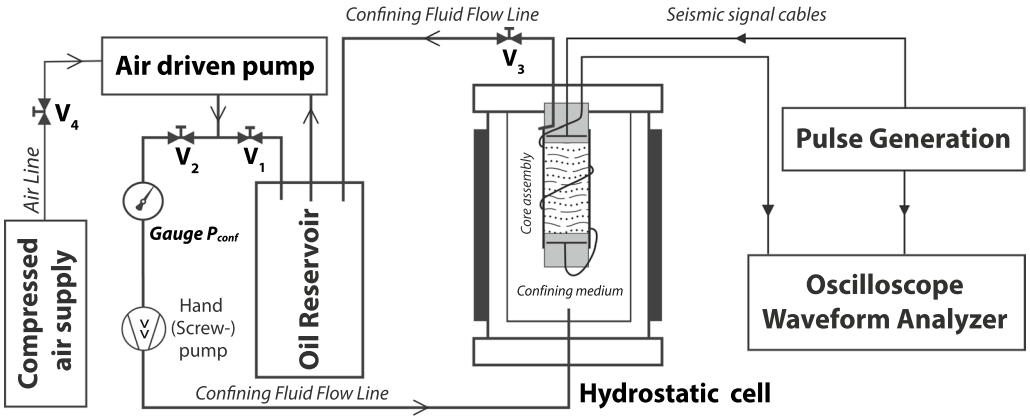

Fig. 4 Schematic setup of the seismic apparatus used to measure ultrasonic velocities up to 260 MPa confining pressure and at room temperature. The core assembly is accommodated inside a hydrostatic vessel, where the oil is the confining medium

3.2 Density, porosity and permeability measurements

Bulk density was calculated by weighting the plugs after dehydration in oven for 24 hours, with a highly precise balance ($\pm 5.0 \times 10^{-7}$ kg tolerance), and determining the bulk volume of the plugs, using a caliper ($\pm 2 \times 10^{-5}$ m accuracy) to measure their length and diameter. The grain density was measured by using a gas displacement He-pycnometer apparatus (Accupyc II 1340, Micromeritics), that measures the matrix volume of the plugs at room conditions. The standard deviation of each measurement was lower than 5%. The effective porosity has been calculated as the difference between grain and bulk density. Fluid permeability measurements were performed using an oil-based hydrostatic pressure medium apparatus (permeameter) developed "in house" based on the transient step method (Brace et al. 1968). Using an automated permeameter–porosimeter (AP-608, Coretest Systems, INC.) at Geneva University, the fluid permeability (Y-plugs) measurements are performed based on the unsteady pressure drop method and Boyle's law (Jones 1972).

3.3 Seismic velocity measurements

Measurements of ultrasound waves propagation were performed at the Rock Physics and Mechanics Laboratory—ETH Zurich, following the pulse transmission method (Birch 1960, 1961) to measure separately the velocities of compressional- and shear-wave as a function of confining pressure (Fig. 4). The pulse transmission method, which is described in detail by Christensen (1985), is based on measuring the travel time of a mechanical impulse through a rock plug, placed between two piezoelectric transducers.

The experiments were performed under two successive cycles of pressurization–depressurization using an oil-medium hydrostatic pressure vessel. The confining pressure was generated using an air-driven fluid pump in conjunction with a compressed air system and was measured within ± 2 MPa precision at the highest pressure. The pressure was incrementally increased up to 260 MPa and subsequently decreased with steps of $\sim$20 MPa. The experiments were performed at room temperature. The plug was placed between two lead zirconate titanate piezoceramic transducers, which were mounted into metal-heads, containing buffer rods, in order to optimize the transmission of mechanical energy towards the plug. The heads and the plug were encapsulated with a double polyolefin heat shrink tube (with an undrained pore space) to avoid contamination of the plug with the oil and to hold the plug in the correct alignment throughout the experiment. Separate P- and S-wave emitters were employed.

We used transducer with 1 MHz resonance frequency, therefore compressional and shear wavelengths were an order of magnitude larger than the grain size observed in the thin sections. The impedance used was 1 MΩ and range was ± 500 mV. The waveforms were collected with a time step of 8×10^{-8} s, and sampling rate of 25 MHz, and the electric noise was minimized by averaging the tracks. All acoustic waveforms during both pressurization and depressurization cycles were transferred to the computer for further processing without loss of resolution. Cables, transducers, and interfaces in the electronic system introduce a delay in the observed traveling time (i.e., $t_{\text{observed}} = t_{\text{rock}} + t_{\text{system}}$), therefore a calibration was performed before velocities measurements and repeated after the data collection phase.

The calibration was performed by measuring the travel time of the ultrasonic impulses (P and S) through steel cylinders of 24 mm, 29 mm, 39 mm and 44 mm in length,

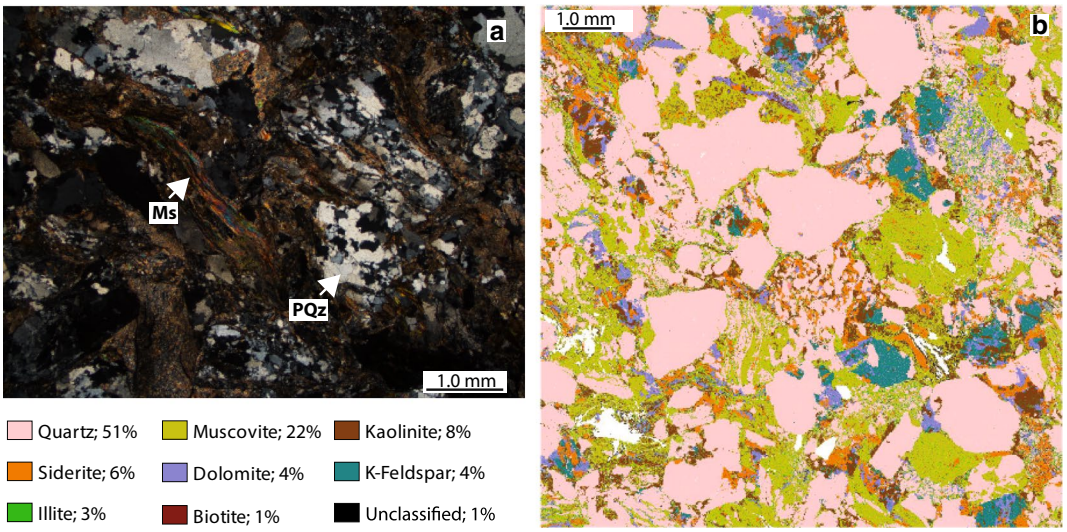

Fig. 5 The preliminary petrographical features of Permo-Carboniferous sediment (sample HU27; depth: 3037.45 m) including documentation of very coarse and partially dissolved detrital polycrystalline quartz grains (PQz) and muscovite (Ms). Stress resulted in the deformation of quartz grains into domains with slightly different extinction angles (left image; **a**). The Kaolinization of K-feldspar is occurring to form the clay cement for pore-filling and grains coating of the component grains; QEMSCAN analysis (right image; **b**). Minerals with volume < 0.5% were not mentioned

plotting the travel times against the cylinders lengths, interpolating linearly the results, and calculating the time value corresponding to zero length. Measurements were conducted at confining pressures of 50 MPa, 100 MPa, and 200 MPa. The traveling time through the system (t_{system}) was obtained by averaging the results obtained for the three different pressures.

4 Results

4.1 Petrography

4.1.1 Permo-Carboniferous sediments (samples HU27 and HU29)

The Permo-Carboniferous is characterized by an alternation of sandstones and shales layers. The sandstone mineralogy exhibits kaolinite sometime affected by illitization (Fig. 5). The large crystal morphology observed are typical of burial diagenesis under high temperatures. Coal chips as well as palynological fossils are commonly found in these sandstone layers.

4.1.2 Lower Triassic (Buntsandstein siliciclastic unit; samples HU25 and HU26)

The Buntsandstein unit is a thin Lower Triassic sandstone (Figure 2) showing many heterogeneities at the microscopic scale (Table 1). It is characterized by green, subrounded, coarse quartz grain. Associated with quartz, the mineralogical composition displays low amounts of K-feldspar (7%) and illite (4%; Fig. 6e). Rarely, quartz grains can present micro-fractures that are filled by diagenetic minerals (Fig. 6f).

4.1.3 Middle Triassic (Muschelkalk and Lettenkhole units; samples HU17–HU24)

The Muschelkalk and Lettenkhole series present alternations of grey dolomitized grainstone with anhydrites nodules and dark, laminated, anhydrite layers. The base of the Muschelkalk is marked by a decrease in clastic sediment input and the presence of glauconite and evaporites. Two microfacies can be observed: (1) a dolomitized grainstone/packstone with peloids, ooids and anhydrite nodules displaying fluid inclusions and (2) peloidal laminated anhydritic layers (HU23, Fig. 6c, d). The dolomitic intervals are also characterized by frequent microcracks and sub-vertical fractures filled with anhydrite.

4.1.4 Upper Triassic (Keuper Formation; Samples BX107, CL126, and GDHlt)

The anhydrite-clay-salt interval (Keuper formation; 2548 to 2896 m depth) was originally not cored at Humilly. Nevertheless, we thought that such horizon could give interesting seismic results and we wanted to test it in laboratory. Therefore, in addition to the twenty-eight samples from HU2 borehole, we obtained an anhydrite sample from Bex-3 borehole in the Canton Vaud (depth of 107.35–108.5 m; Ultrahelvetic Zone, Bex-Laubhorn-Nappe, Switzerland).

The horizontal plug shows vein networks filled by anhydrite (0.3–0.7 mm), cleavage surface and brecciation. For the clay component we considered literature data referring to sample CL126 (Freund 1992); it is a claystone from Salzwedel 2/64 borehole,

Table 1 Modal composition, determined using the automatic QEMSCAN-analysis (Gottlieb et al. 2000)

Core	Sample	Depth (m)	Rock-type (age)	Formation name	Modal composition (%)
Core I	HU01	1015.0	Limestone (Upper Jurassic)	*Kimmeridgian Reef Complex*	100 Cal
	HU03	1018.1			100 Cal
	HU06	1020.1			100 Cal
Core II	HU07	1853.4	Limestone (Upper Jurassic)		96 Cal, 2 Qz, 1 Oth, 1 Ucf
	HU08	1857.3			96 Cal, 1 Dol, 1 Ilt, 1 Qz, 1 Oth
	HU09	1860.8			91 Cal, 2 Ilt, 2 Qz, 2 Ucf, 1 Bt, 1 Dol, 1 Oth
	HU10	1997.8			90 Cal, 7 Qz, 3 Ucf
	HU11	2001.4			91 Cal, 6 Qz, 2 Ucf, 1 Dol
	HU12	2003.5			87 Cal, 9 Qz, 3 Ucf, 1 Oth
Core III	HU13	2242.7	Shale		28 Qz, 20 Cal, 9 Dol, 7 Bt, 30 Ilt, 2 Chm, 2 Glt, 1 Pl, 1 Oth
	HU14	2468.3	Limestone (Lower Jurassic)		96 Cal, 1 Dol, 2 Qz, 1 Ucf
	HU15	2472.9			91 Cal, 3 Qz, 3 Ilt, 3 Oth
Core IV	BX107[a]	2630.0	Anhydrite-Claystone-Halite (Upper Triassic)	*Keuper*	75 Anh, 15 Mgs, 5 Qz, 2 Gp
	CL126[b]	2710.0			87 Ilt/Kln, 11 Qz, 1 Anh,
	GDHlt[c]	2770.0			100 Hl
Core V	HU17	2905.5	Dolomite Anhydrite (Middle Triassic)	*Lettenkohle*	77 Dol, 20 Gp/Anh, 2 Oth, 1 Qz
	HU18	2905.5		*Muschelkalk*	96 Dol, 2 Gp/Anh, 1 Qz, 1 Oth
	HU19	2916.6			54 Dol, 45 Gp/Anh, 1 Qz
	HU20	2922.5			54 Gp/Anh, 45 Dol, 1 Qz
	HU21	2930.3			68 Dol, 27 Gp/Anh, 1 Cal, 1 Qz, 3 Oth
	HU22	2951.4			68 Dol, 31 Gp/Anh, 1 Oth
	HU24	2967.0			65 Dol, 34 Gp/Anh, 1 Qz
	HU25	3028.3	Sandstone (Lower Triassic)	*Buntsandstein*	86 Qz, 7 Kfs, 4 Ilt, 1 Ms, 2 Oth
	HU26	3030.2			84 Qz, 12 Kfs, 2 Ilt, 1 Kln, 1 Ms
	HU27	3037.5	Sandstone (Permo- Carboniferous)		51 Qz, 22 Ms, 8 Kln, 6 Sd, 4 Dol, 4 Kfs, 3 Ilt, 1 Bt, 1 Ucf
	HU29	3038.8			39 Qz, 20 Bt, 11 Kln, 8 Ilt, 7 Chm, 6 Sd, 6 Ucf, 2 Glt, 1 Dol

Data for Core IV were not sampled in Humilly but derive from literature accordingly to references a, b and c. Mineral abbreviations are after Whitney and Evans (2010): *Bt* Biotite, *Cal* Calcite, *Chm* Chamosite, *Dol* Dolomite, *Glt* Glauconite, *Gp/Anh* Gypsum/Anhydrite, *Hl* Halite, *Ilt* Illite, *Kln* Kaolinite, *Kfs* K-Feldspar, *Mgs* Magnesite, *Ms* Muscovite, *Oth* Other, *Pl* Plagioclase, *Qz* Quartz, *Sd* Siderite *Ucf* unclassified

[a] After Müller and Briegel (1977)

[b] After Freund (1992)

[c] After Yan et al. (2016)

(Sachsen-Anhalt, Germany) collected at a depth of 3466 m in the Rotliegend Formation. For the salt component we used data from Yan et al. (2016) referring to a halite sample from the Napoleonville salt dome, Assumption Parish, Louisiana, USA collected at a depth of 300 m.

4.1.5 Lower Jurassic (Liassic mixed units; samples HU13–HU15)

The Lower Jurassic at HU2 borehole is represented by a lower carbonate unit and an upper clay-rich unit. The lower unit is composed by very fine-grained homogeneous micrite (> 91% calcite) associated with microbial structures. A few shell fragments (mainly foraminifera) are preserved as molds filled with diagenetic calcite (Samples HU14, 2468.25 m depth; Fig. 6b). The upper unit is composed predominantly by clay minerals (30% illite) and quartz (28%), and fine-grained calcite (20%) with abundant mica (7% biotite), dolomite (9%), and other silt-size minerals (Fig. 6a).

4.1.6 Middle Jurassic (Dogger limestone unit; samples HU07–HU12)

The Dogger unit is about 315 m thick in HU2 but the Liassic-Dogger transition is arbitrarily set at the clear distinction between the Upper Liassic unit of bioclastic Mudstone–Wackstone and the first presence of mica-rich limestones (Fig. 7c). The middle and upper part of

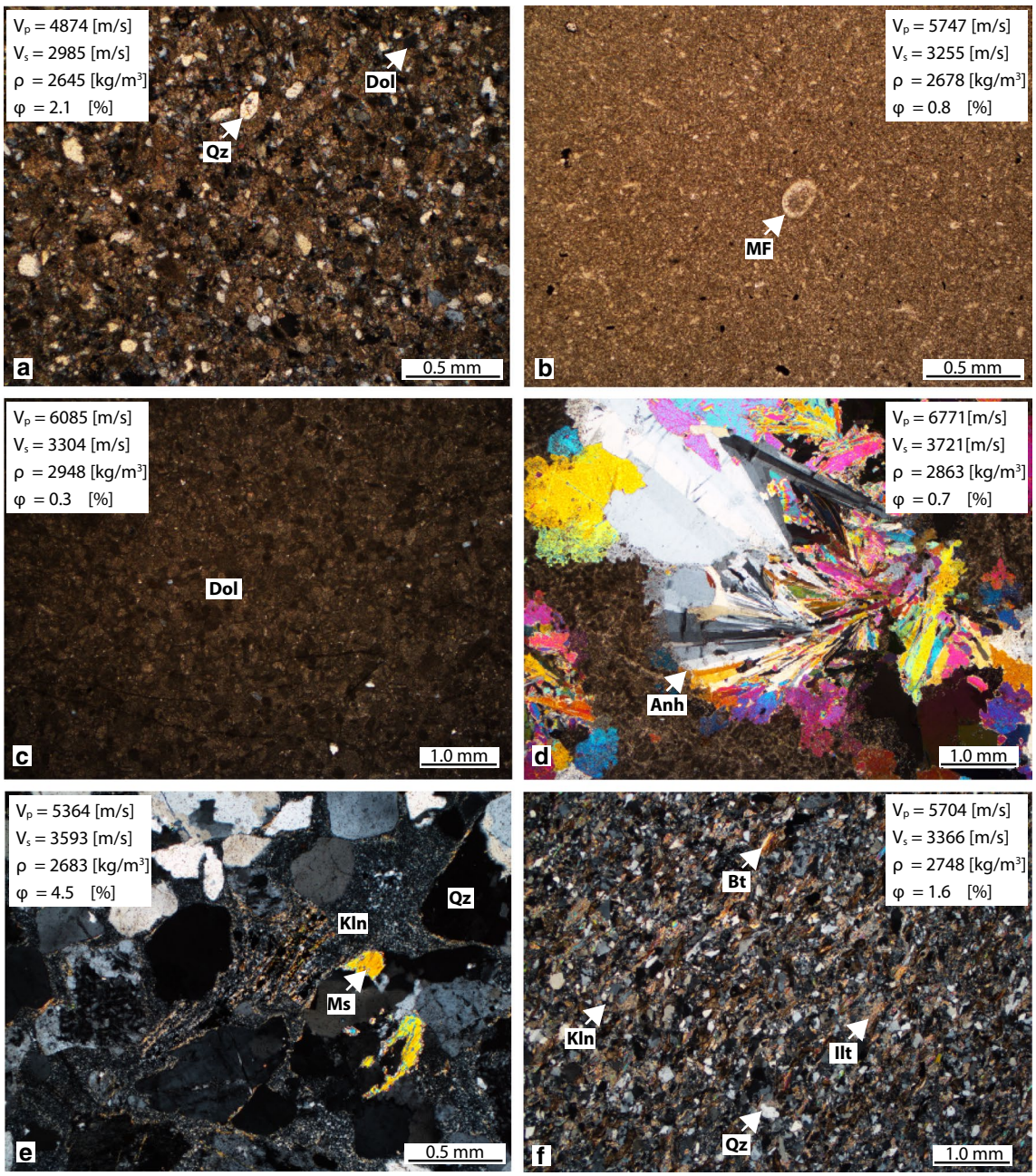

Fig. 6 Representative optical photomicrograph showing: **a** sample HU13; Pliensbachian—Posidonia shale. A considerable fine quartz (Qz) sand content exceeds 27% in volume are embedded in micrite 'composed of 1–4 μm-sized clay mineral'. Fine-crystalline dolomite (Dol) rhombs are embedded in the mud matrix; sample HU-13. **b** sample HU14; Sinnemurian—very fine-grained homogeneous micrite (> 91% calcite). A few of shell fragment (benthonic forams) which are preserved as a mold (MF) and filled with mostly diagenetic calcite, are embedded within very fine-grained homogeneous micrite. **c** sample HU21; Triassic Muschelkalk shows the microcrystalline micrite-dominated dolostone (fine-crystalline dolostone (Dol). **d** sample HU24; Triassic Muschelkalk presents the abundance of fibrous anhydrite (Anh) as the evaporite minerals in dolomitic (Dol) carbonate-support. **e** sample HU25; Triassic Buntsandstein. The kaolinization (Kln) of K-feldspar (Kfs) is occurring to form the clay cement for pore-filling and grain-coating on Quartz (Qz) minerals. Micro-fractures in quartz grains are not so common and filled by later diagenetic minerals. **f** sample HU29; Permo-Carboniferous unit. It shows slight laminations of fine-quartz (Qz) grains associated with kaolinite and biotite (Bt). The preservation of detrital feldspar and clay minerals (background) significantly contribute in the reduction of the porosity (0.87 ± 0.16%)

the Dogger are mainly composed of bioclastic grainstone with dominant heterozoan assemblages, and sparse detritic quartz grains (maximum 1% of total allochem amount, Fig. 7d, e).

4.1.7 Upper Jurassic (Kimmeridgian Reef Complex unit; samples HU01–HU06)

The Upper Jurassic is more than 1000 m thick in HU2. The lithology is heterogeneous, ranging from marls to pure carbonates. This unit is often affected by various types of dolomitization from simple slight dolomitization in the form of fine dolomite crystals to fabric-destructive, sucrosic, dolomitization. The base of the Upper Jurassic displays a dark grey, bioclastic, marly limestone with few darker marl intervals. The Upper Jurassic limestone displays a white, massive, bioclastic limestone, with a 15 cm thick dolomitic interval at the base. The successive microfacies observed include at the base microbial boundstone, alternating with bioclastic grainstone to rudstone, whose bioclasts show large micrite envelopes that can sometimes prevent their identification (Fig. 7a, b) but are mainly composed of echinoderms, lamellibranchs, gastropods and foraminifers. Microbial constructions are then progressively replaced by coral framestone, still intercalated with bioclastic grainstone to rudstone. Moldic dissolution features, intra/inter-particle pores, and fractures are systematically filled with calcitic cement.

4.2 Modal composition, density, porosity and permeability

The results of the mineralogical mapping, using QEMSCAN analysis are shown in Table 1 [the data available in Hefny et al. (2020)]. The mineral composition of the anhydrite-clay-halite section derived from literature (Freund 1992; Müller and Briegel 1977; Yan et al. 2016) are also reported in Table 1. Grain density, effective porosity, and fluid permeability data are given in Table 2. The full dataset is made available by Hefny et al. (2020).

The Upper Jurassic section is characterized by monomineralic limestones while the Middle and Lower Jurassic limestones show a more complex mineralogy, with quartz in variable percentages up to 9%, and minor dolomite, illite and biotite. The Triassic dolomitic section of Muschelkalk/Lettenkhole present generally abundant Gypsum/Anhydrite, up to 54% in sample HU20, and minor quartz (around 1%). The siliciclastic units in the deepest part of the borehole are represented either by quartz rich sandstones (Buntsandstein), or fine grained to argillaceous quartz rich sediments (Permo-Carboniferous unit).

In the Upper Jurassic limestone Reef Complex unit, the grain density average is 2720 ± 19 kg/m^3, reflecting the homogeneous mineralogical composition of the samples. Effective porosity ranges from 10.15 ± 0.4 to 16.65 ± 0.15% while permeability ranges from 3.9×10^{-16} to 9.08×10^{-16}m^2, representing the highest values we could measure in our sequence. No relevant variation is observed between permeability measurements parallel or perpendicular to bedding. Porosity and permeability increase from top to the bottom of the Upper Jurassic limestone section.

In the Dogger limestone unit, the average grain density is 2714 ± 19 kg/m^3, therefore similar to the limestones of the Upper Jurassic. The porosity is significantly lower than in the Upper Jurassic limestone Reef Complex, varying from 1.53 ± 0.15 to 2.72 ± 0.16%. The maximum permeability measured 3.6×10^{-16}m^2, was found in the X direction of sample HU07, in the upper part of the sequence, but most of the samples in the sequence show permeability values lower than the minimum value detectable with our instruments.

The Liassic shales at 2242.7 m depth has an average grain density of 2657 kg/m^3, therefore slightly lower than the limestone in the same sequence, but equal porosity (2.1 ± 0.2%) and permeability below detectability. The Liassic limestones are also characterized by a low porosity; the maximum value is 2.42 ± 0.4%, observed along the bedding plane of sample HU15 (argillaceous limestone). Permeability is also very low: 10^{-18} m^2 along the bedding plane and below the detection capability of our instrument perpendicular to bedding. Density (kg/m^3) values are typical of limestone and vary from 2678 ± 2 to 2723 ± 3. The mineral composition of the anhydrite sample (BX126) is 75.4% anhydrite, 15% magnesite, 5% quartz and 2% gypsum (Müller and Briegel 1977). Data reported in literature Gassmann et al. (1979) for density and porosity are respectively 2910 ± 10 kg/m^3 and 0.58 ± 0.2%.

The Muschelkalk-Lettenkohle anhydrite-dolomites show the lowest effective porosity of the whole samples set, with values ranging from 0.28 ± 0.11 to 1.65 ± 0.09%. The only value of the permeability we could determine was $4.0 \pm 0.7 \times 10^{-19}$m^2 corresponding to plug HU24X at a depth of 2967 m. The presence of abundant dolomite and anhydrite determines a relatively high grain density compared to the other units in the sedimentary sequence, with average values of 2887 ± 34 kg/m^3.

The density values of Buntsandstein sandstones unit are lower than the overlying Muschelkalk formation, while porosity and permeability are higher. The average density is 2655 ± 18 kg/m^3. Porosity ranges from 2.09 ± 0.27 to 4.50 ± 0.21%. The permeability values range from $0.4 \pm 0.1 \times 10^{-18}$ to 54.0×10^{-18}m^2, with values perpendicular to banding one order of magnitude lower than the measured values in the bedding plane.

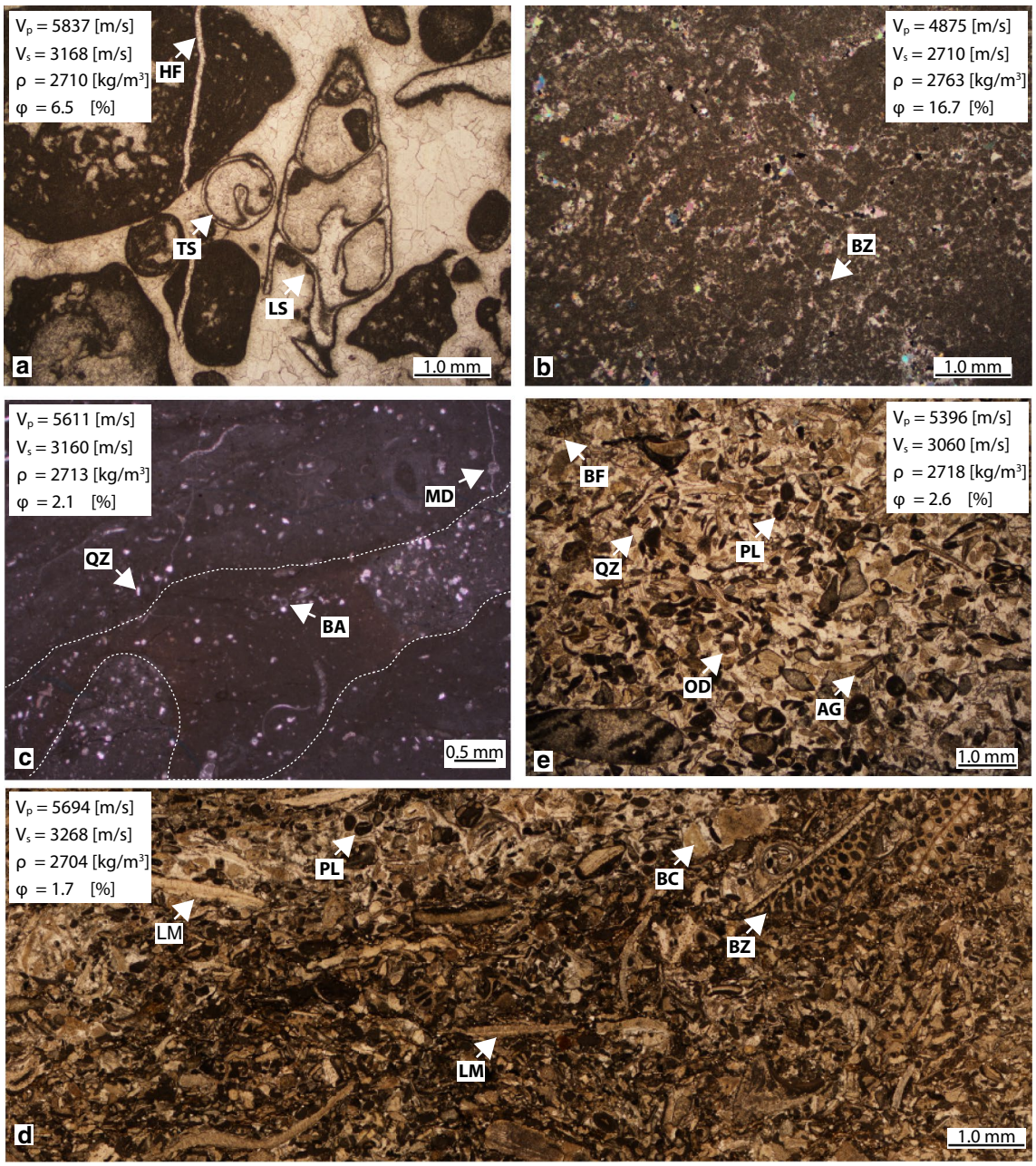

Fig. 7 Optical photomicrograph of representative samples: **a** and **b** sample HU01; Upper Jurassic Carbonate section. A wide abundance of tubiphytes (TP), bryozoans (BZ), sponge/algae reefs (SG), and mollusca debris (mainly gastropods) were observed. Well-preserved longitudinal (LS) and transversal (TS) cross-sections of a high-spired gastropod show spar-infilled chambers and internal cavities, while the external outline is micritic sediment. Fractures (HF) were filled by a sparite cement. **c** sample HU07; Bathonian—bioclastic Mudstone-Wackstone unit. Bioclasts, including benthonic forams such as miliolids (MD), echinoderms and bioclastic algae (BA), are embedded in a micritic or peloidal calc-mud matrix; Diagenetic or post-depositional features including the formation of horsetail stylolites due to compaction were observed. **d** sample HU09; Bathonian—Benthic Crinoidal Packstone unit, where Benthonic Crinoidal (BC), bryozoa (BZ), and Lamellibranchs (LM) fragments representing the most abundant component. **e** sample HU12; Bajocian—Peloidal Packstone-Grainstone unit, showing abundance of foraminifers bioclasts (BF), algae (AG), peloids (PL) and few ooids (OD)

Table 2 Summary of the grain density; ρ_{grain} (kg/m^3), effective porosity; ϕ_{eff} (%), and permeability; k (m^2) for the studied plugs

Core	Sample	ρ_{grain} (kg/m^3)			ϕ_{eff} (%)			k ($\times 10^{-18}$ m^2)		
		X-direction	Y-direction	Z-direction	X-direction	Y-direction	Z-direction	X-direction	Y-direction	Z-direction
Core I	HU01	NA	2710 (5)	2709 (1)	NA	12.5 (0.7)	10.2 (0.4)	NA	*508*	389 (5)
	HU03	2715 (2)	NA	2722 (2)	12.8 (0.1)	NA	13.0 (0.1)	586 (15)	NA	436 (5)
	HU06	2763 (3)	2710 (3)	2714 (2)	16.7 (0.2)	13.1 (0.2)	14.9 (0.2)	719 (16)	*752*	908 (21)
Core II	HU07	2713 (2)	2696 (2)	2713 (2)	2.1 (0.1)	1.3 (0.3)	2.0 (0.2)	358 (5)	*236*	0.9 (0.1)
	HU08	2738 (3)	2726 (1)	2735 (3)	2.6 (0.2)	0.9 (0.1)	2.3 (0.2)	*0.987*	BL	*0.987*
	HU09	2718 (2)	2725 (3)	2728 (3)	2.6 (0.2)	2.9 (0.4)	2.7 (0.2)	*11.8*	*3.3*	*0.987*
	HU10	2708 (0)	2707 (1)	2713 (2)	1.3 (0.2)	1.5 (0.3)	2.3 (0.4)	BL	*2.0*	BL
	HU11	2714 (1)	2704 (1)	2712 (1)	1.7 (0.2)	1.4 (0.2)	1.5 (0.2)	BL	*1.0*	3.948
	HU12	2704 (1)	2701 (1)	2711 (2)	1.7 (0.3)	1.3 (0.2)	1.8 (0.1)	0.2 (0.0)	*1.0*	BL
Core III	HU13	2645 (3)	NA	2669 (1)	2.1 (0.2)	NA	2.1 (0.2)	BL	NA	BL
	HU14	2678 (2)	2680 (1)	2687 (1)	0.8 (0.2)	0.2 (0.5)	0.3 (0.1)	BL	BL	BL
	HU15	2708 (3)	2723 (3)	2688 (1)	1.5 (0.2)	2.4 (0.4)	0.6 (0.2)	BL	*1.0*	BL
Core IV	BX107	2839 (3)	NA	2893 (3)	9.5 (0.7)	NA	5.4 (1.0)	910.9	NA	11.84
Core V	HU17	2946 (2)	2852 (1)	2938 (2)	0.5 (0.3)	0.3 (0.1)	0.6 (0.3)	BL	BL	BL
	HU18	2863 (3)	2858 (1)	2859 (2)	1.4 (0.2)	1.5 (0.2)	1.7 (0.1)	1.974	*38.49*	461.9
	HU19	2869 (2)	2852 (1)	2877 (3)	0.8 (0.3)	0.3 (0.1)	0.4 (0.2)	*0.987*	*0.3*	BL
	HU20	2850 (2)	2842 (1)	2891 (1)	0.7 (0.4)	0.6 (0.3)	0.9 (0.2)	BL	BL	BL
	HU21	2948 (1)	2925 (0)	2933 (1)	0.3 (0.1)	0.3 (0.0)	0.5 (0.2)	BL	BL	BL
	HU22	2877 (2)	2878 (1)	2894 (1)	0.7 (0.1)	0.6 (0.1)	0.8 (0.1)	BL	BL	10.86
	HU24	2863 (2)	2903 (2)	2909 (2)	0.7 (0.1)	0.4 (0.1)	0.7 (0.2)	0.4 (0.1)	BL	BL
	HU25	2683 (3)	2663 (2)	2661 (4)	4.5 (0.2)	3.7 (0.4)	3.6 (0.3)	3.9 (0.9)	*3.0*	0.6 (0.2)
	HU26	2640 (2)	2655 (3)	2630 (1)	2.1 (0.3)	3.1 (0.2)	2.5 (0.3)	6.5 (0.3)	*54*	0.4 (0.1)
	HU27	2772 (3)	2772 (2)	2779 (3)	2.9 (0.2)	2.4 (0.5)	2.4 (0.2)	34.3 (2.5)	*47.7*	4.4 (5.0)
	HU29	2748 (3)	2725 (3)	2732 (1)	1.6 (0.2)	1.3 (0.3)	0.9 (0.2)	0.5 (0.3)	*2.0*	BL

Standard deviations inside parentheses are expressed in units of the last digit. The permeability measurement performed at Geneva University are in italic

NA not available, *BL* below limit (lower limit = 9.87 $\times$ 10^{-20}m^2), *NM* Not Measured

Permo-Carboniferous sediments at the bottom of the borehole have average density of 2755 $\pm$ 20 kg/m^3 while permeability and porosity are in the same range as for Buntsandstein.

4.3 Seismic velocities

The seismic velocities were calculated using Eq. (1), where L is the plug's length, t_{rock} is the traveling time of either P- or S-wave through the rock plug, and $\delta V_{p,s}$ is the uncertainty of V_p or V_p propagation through the experiments, respectively. No correction for length variation during pressurization was necessary, samples length was measured before and after pressurization to make sure that no permanent deformation was induced. The experimental traveling time of either P- or S-wave through the rock plug under loading/unloading cycles (i.e. up to 260 MPa confining pressure measurements) are available in Hefny et al. (2020). The first arrival times of P- and S-wave were manually picked using a MATLAB code developed for that purpose (Grab et al. 2015), with $\pm 2 \times 10^{-9}$ second precision.

$$V_{p,s} = \frac{L}{t_{rock}} \pm \delta V_{p,s}, \tag{1}$$

Figure 8 is an example of a typical experimental curve of compressional velocity variation during a two pressurization/depressurization cycles. The seismic velocities-confining pressure curves show a typical non-linear relationship at lower confining pressure, typically below 150–180 MPa, (in the example of Fig. 8 it is 175 MPa), attributed to crack closure. The linear portion, at higher pressure, reflects the intrinsic seismic properties in the selected direction of the rock under consideration (Birch 1960, 1961). The linear regression of the data measured between 150 and 250 MPa was used to calculate velocity reference values at room pressure for P- and S-waves respectively. The intercept of the linear regression is referred as $V_p(0)$ and $V_s(0)$, i.e. $V_{p,s}$ at zero pressure, and

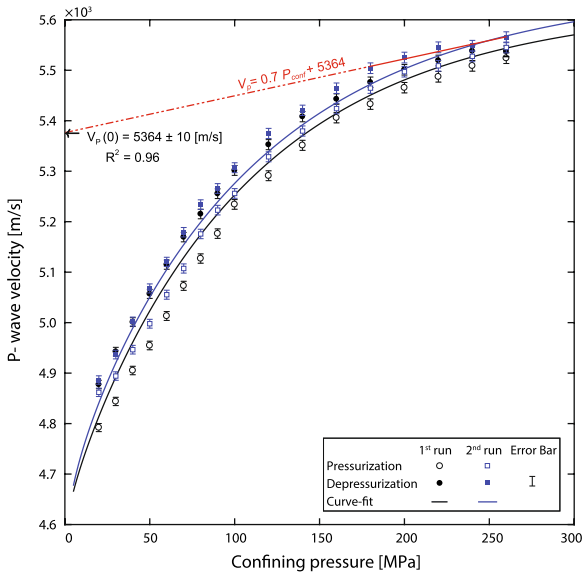

Fig. 8 Example of two cycles of pressurization–depressurization of compressional-waves (sample HU25X). The non-linear velocity/pressure correlation at low pressure (up to ca. 175 MPa) is due to the closure of cracks/pores. The linear velocity/pressure correlation is due to intrinsic compressibility elastic moduli of the mineral skeleton of the rock. The velocity measurements during the depressurization run (filled symbols) show larger values than those obtained during the pressurization runs (empty symbols). This effect (hysteresis) is interpreted as due to the only partial re-opening of fractures and microcracks that close during pressurization. The intrinsic velocity $V_p(0)$ was calculated by the linear regression (red line) intersection of the high-pressure part of the second depressurization 2nd run back to the zero-confining pressure. These coefficients of the linear regression are corresponding to the pressure derivative of velocities. The fitting curve was calculated on the 2nd complete run using the Wepfer and Christensen (1991) equation

the slope of the linear regression represents the pressure derivative.

According to Burke and Fountain (1990), only measurements taken during depressurisation are reproducible within error limits. Therefore, we used only the depressurization cycles to calculate V_0. We estimated the error ($\delta V_{p,s}$) for each velocity by using Equ. (2) (Taylor 1997).

$$\delta V_{p,s} = \sqrt{\left(\frac{\partial V_{p,s}}{\partial L}\delta L\right)^2 + \left(\frac{\partial V_{p,s}}{\partial t_{observed}}\delta t_{observed}\right)^2 + \left(\frac{\partial V_{p,s}}{\partial t_{system}}\delta t_{system}\right)^2}$$
$$= \sqrt{\left(\frac{1}{t_{observed} - t_{system}}\delta L\right)^2 + \left(\frac{-L}{(t_{observed} - t_{system})^2}\delta t_{observed}\right)^2 + \left(\frac{t_{system}}{(t_{observed} - t_{system})^2}\delta t_{system}\right)^2} \quad (2)$$

$\partial V_{p,s}/\partial L$, $\partial V_{p,s}/\partial t_{observed}$, and $\partial V_{p,s}/\partial t_{system}$ are the partial derivative of the seismic velocities with respect to the plug's length (L), the observed travel time ($t_{observed}$), and the travel time through the system (t_{system}), respectively. δL is the standard deviation of the plug's length, measured using a digital caliper with 2×10^{-5}m accuracy. $\delta t_{observed}$ is the uncertainty in the picking of the first arrival on the waveform, and it is the main source of error in the determination of seismic velocity. We estimated a typical uncertainty in the picking both for P- and S-wave in the order of magnitude of $\delta t_{observed} \simeq \pm 2 \times 10^{-9}$s. From the calibration of seismic rig (Sect. 3.3), we calculated a $\delta t_{system} = \pm 1.4794 \times 10^{-8}$s, and $\pm 1.9341 \times 10^{-8}$ for V_p and V_s, respectively. The uncertainty has nearly the same size as the symbol used in the Figures, at most ~27 m/s, and therefore not visible in the diagrams. Velocity data are presented in Table 3.

Average V_{p0} velocities (m s^{-1}) range from 4897 to 5897 for limestone with the highest values in the middle Jurassic samples, from 5979 to 6648 for dolomite, and from 5303 to 5646 in sandstones. V_{s0} velocities (m s^{-1}) range from 2759 to 3267 for limestone, from 3293 to 3737 for dolomite, and from 3336 to 3591 in sandstones. The only shale in our collection has a maximum value of 4775 and 2901 for V_{p0} and V_{s0}, respectively. The anhydrite rich sample from BEX has an average velocity of 4813 and 2859 for V_{p0} and V_{s0}, respectively .

4.4 Seismic anisotropy and Vp/Vs ratio

Velocities measured along mutually perpendicular directions, parallel and perpendicular to banding, were used for calculating the seismic anisotropy $AV_{p,s}$ (%) of the rocks as in Eq. (3).

$$AV_{p,s} = \frac{V_{p,s}^{max} - V_{p,s}^{min}}{V_{p,s}^{mean}} \times 100 \pm \delta AV_{p,s}, \quad (3)$$

Table 3 Summary of intrinsic seismic velocities (m/s) for compressional- V_{p0}, and and shear-waves V_{s0}, anisotropy (%) for compressional- (AV_p) and shear-waves (AV_s), Thomsen parameters ϵ and γ, and V_pV_s ratio

Core	Sample	Compressional velocity; V_{p0} (m/s)				AV_p (%)	ϵ (–)	Shear velocity; V_{s0} (m/s)				AV_s (%)	γ (–)	V_pV_s
		X-direction	Y-direction	Z-direction	Average			X-direction	Y-direction	Z-direction	Average			Ratio
Core I	HU01	NA	5140 (27)	5411 (11)	5276	5.14	0.082	NA	2927 (15)	2969 (5)	2948	1.42	0.069	1.79
	HU03	5136 (10)	NA	5109 (10)	5123	0.53	0.004	2808 (4)	NA	2851 (4)	2830	1.52	−0.016	1.81
	HU06	4875 (09)	4952 (10)	4865 (08)	4897	1.78	0.011	2710 (4)	2845 (4)	2722 (4)	2759	4.89	0.021	1.78
Core II	HU07	5611 (12)	5876 (16)	5570 (13)	5686	5.39	0.008	3160 (5)	3127 (5)	3095 (5)	3127	2.08	0.021	1.82
	HU09	5396 (11)	5402 (14)	5361 (14)	5386	0.76	0.005	3060 (5)	3033 (6)	3029 (6)	3041	1.02	0.009	1.77
	HU12	5694 (13)	5797 (17)	5705 (12)	5732	1.8	0.045	3268 (6)	3261 (8)	3272 (5)	3267	0.34	−0.003	1.75
Core III	HU13	4874 (10)	NA	4675 (08)	4775	4.16	0.039	2985 (5)	NA	2817 (4)	2901	5.79	0.056	1.65
	HU14	5747 (15)	5970 (27)	5974 (13)	5897	3.85	−0.002	3255 (6)	3228 (5)	3243 (5)	3242	0.83	0.002	1.82
Core IV	BX107	4339 (20)	NA	5286 (23)	4813	19.68	−0.169	2765 (13)	NA	2953 (12)	2859	6.58	−0.07	1.68
Core V	HU17	6152 (13)	6144 (13)	6160 (14)	6152	0.26	0	3422 (6)	3413 (5)	3431 (6)	3422	0.53	−0.001	1.80
	HU20	6785 (16)	6762 (19)	6396 (14)	6648	5.85	0.055	3790 (7)	3754 (8)	3668 (6)	3737	3.26	0.026	1.78
	HU21	6085 (14)	6100 (16)	5752 (14)	5979	5.82	0.062	3304 (6)	3293 (0)	3282 (6)	3293	0.67	0.009	1.82
	HU24	6771 (16)	6455 (17)	6630 (16)	6619	4.77	0.013	3721 (7)	3558 (7)	3504 (6)	3594	6.04	0.055	1.84
	HU25	5364 (10)	5314 (11)	5230 (18)	5303	2.53	0.03	3593 (6)	3569 (6)	3612 (12)	3591	1.2	−0.001	1.48
	HU26	5519 (11)	5504 (12)	5580 (16)	5534	1.37	0.009	3545 (6)	3508 (6)	3709 (9)	3587	5.6	−0.041	1.54
	HU27	5673 (13)	5658 (14)	5607 (13)	5646	1.17	0.011	3498 (7)	3362 (6)	3369 (6)	3410	3.99	0.037	1.66
	HU29	5704 (12)	5445 (15)	5492 (11)	5547	4.67	0.043	3366 (5)	3408 (9)	3233 (5)	3336	5.25	0.045	1.66

Errors, inside parentheses, are in units of the last digit

NA Not available

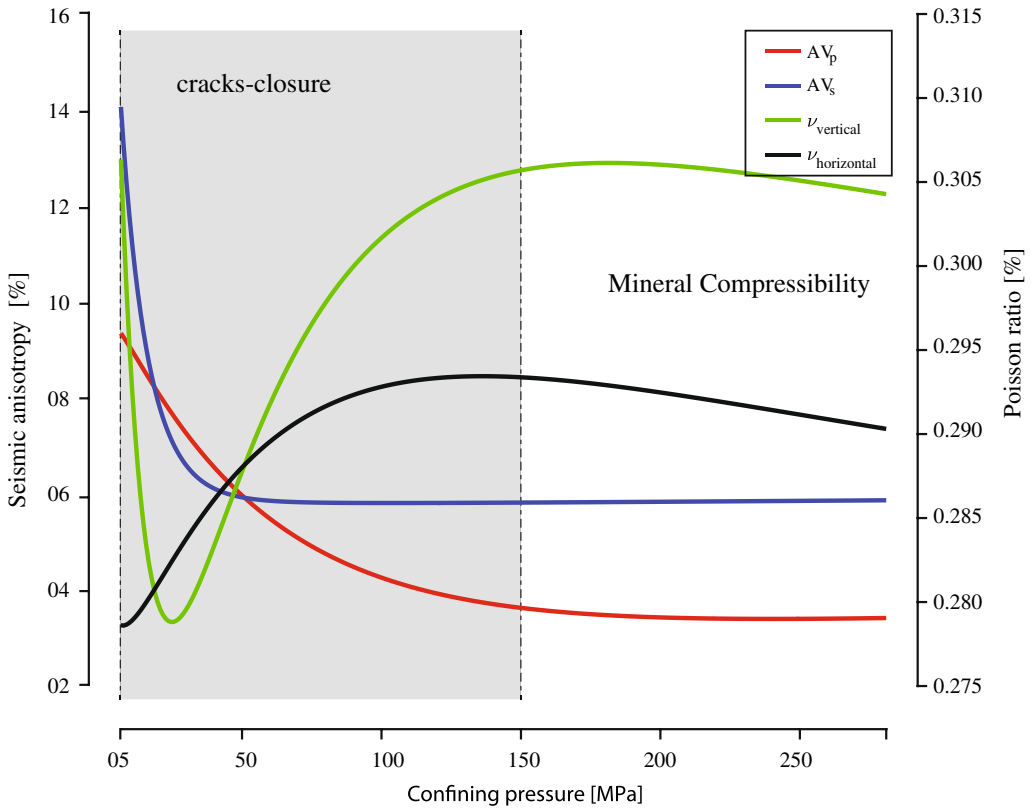

Fig. 9 Example of seismic velocity anisotropy and Poisson's ratio as a function of confining pressure up to 300 MPa. The curves are inter- and extrapolated from laboratory measurements using the equation of Wepfer and Christensen (1991). The plot is split into two areas, on the basis of the linearity of the curves. The low-pressure zone, where the curves are non-linear, represents the pressure interval where the seismic behavior is dominating by crack and pore closures (e.g., Birch 1960). It shows an abrupt decrease due to the closure of the aligned microcracks which reinforce the anisotropy induced by the lattice-preferred orientation (LPO) of anisotropic minerals (sample: HU24). Above 150 MPa, the curves become linear; the elastic behavior of the rocks is determined by the elastic moduli of the rock-forming minerals

Table 3 presents the anisotropies calculated on V_{p0} Vp0 and V_{s0} Vs0, and the respective errors. The seismic velocities measured along the horizontal X-direction plugs are mostly higher than those measured along the vertical Z-direction (perpendicular to the bedding planes). Nonetheless , in some cases, the vertical seismic velocities are sporadically higher than the horizontal one. In general, the samples show very weak anisotropy. The only exception is anhydrite, in fact the maximum anisotropy was found in BX107 with 19.68% and 6.59% for the compressional- and shear-wave seismic anisotropy, respectively. The dolomite-anhydrite samples of the Muschelkalk section also show relatively high P-wave anisotropy (4.77 to 5.85%). Some limestones such as HU01 and HU07 show a relatively high P-wave anisotropy (5.14 and 5.39% respectively), while in general limestone have a lower average anisotropy for P- and S-wave. The Lettenkohle dolomite sample shows the lowest value of 0.26% and 0.51% for the compressional- and shear-wave anisotropy, respectively.

Like seismic velocities, anisotropy tends towards linearity for confining pressures above 150–180 MPa. Figure 9 shows one example of anisotropy calculated from the fitting curves of the sample HU24. The anisotropy at low pressure is generally much higher than the high-pressure zone, indicating that the cracks give a contribution to the anisotropy of the solid skeleton of the rocks.

In addition to anisotropy, we calculated the parameters ϵ, and γ as defined by Thomsen (1986) for a Vertical Transverse Isotropy (VTI) symmetry case. Thomsen parameters are often used in oil and gas industry literature to describe low anisotropy formations in a synthetic and simplified way. P- and S-wave moduli are represented in the general form $c_{xx} = \rho V^2$, where c is the rock stiffness. The P-wave anisotropy parameter (ϵ) measures the difference of P-wave velocity between vertical and horizontal directions; Eq. (4). Similarly, the S-wave anisotropy parameter (γ) measures the difference in S-wave propagation in the vertical and horizontal directions; Eq. (5). The P-wave moduli for the minimum velocity direction perpendicular to the foliation

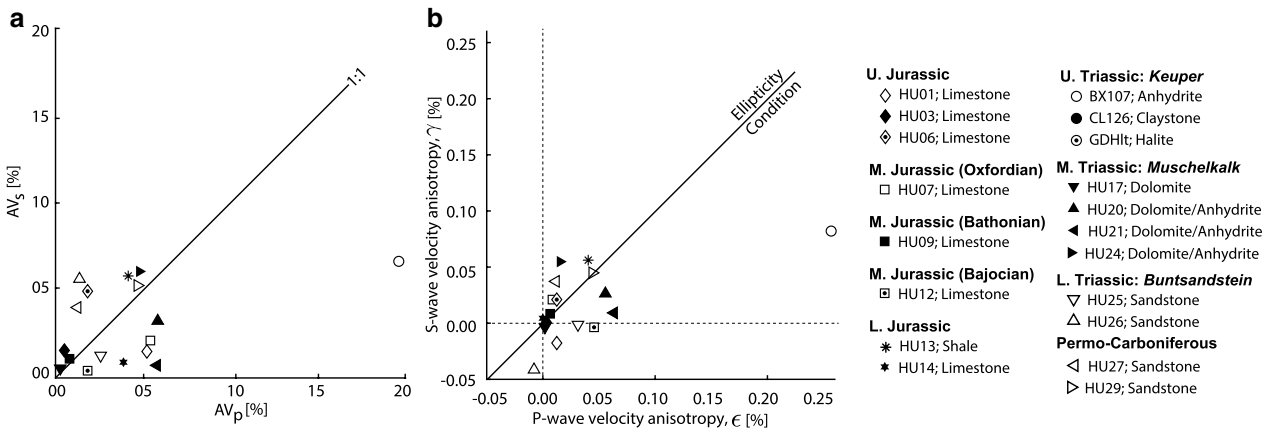

Fig. 10 Cross-plots of **a** P-wave and S-wave velocity anisotropy as a percentage **b** P-wave (ϵ) and S-wave (γ) velocity anisotropy parameters expressed as percentages. Error bars for ϵ and γ are too small to be visible. Note negative values

(Z) and maximum direction parallel to banding (X) plugs are represented by c_{33} and c_{11}, respectively. In order to calculate the c_{11} component, when we used the maximum velocity, which in most of the cases is measured in the bedding plane. The bedding parallel and perpendicular S-wave moduli are represented by c_{66} and c_{44}, respectively.

$$\varepsilon = \frac{c_{11} - c_{33}}{2c_{33}}, \tag{4}$$

$$\gamma = \frac{c_{66} - c_{44}}{2c_{44}}, \tag{5}$$

The calculated Thomsen parameters are reported in Table 3 and plotted in Fig. 10b.

Figure 10a shows the relation between anisotropy of compressional and shear waves. While sandstones tend to be more anisotropic in the shear component (with the exception sample HU25), the anhydrite (BX-107) and dolomites show a higher anisotropy of P waves (with exception of sample HU24). Limestones are scattered in the plot. The V_p/V_s ratio is reported in Table 3 and has been calculated from the V_0 of compressional and shear waves. Dolomites and limestones show the highest ratios and sandstones the lowest, with the lowest values for the Buntsandstein formation.

4.5 In-situ conditions

In order to calculate seismic parameters at in-situ conditions we calculated lithostatic and geothermal gradients for the Humilly borehole. Lithostatic pressure, as well as the geothermal gradient, were calculated for the depth interval of the borehole. Equation (6) was used to determine the derivative of the lithostatic pressure (MPa), and to calculate the in-situ pressure for each plug at depth (m), where ρ is the bulk density [derived from density log; (kg m^{-3})], and g is the constant of acceleration due to gravity (m s^{-2}).

$$\int_0^z \frac{\partial P_{\text{conf}}}{\partial z} = \rho_z g \int_0^z z dz, \tag{6}$$

The maximum lithostatic pressure calculated at the bottom of the borehole is 87 MPa.

The geothermal gradient in the Geneva Basin, following Chelle-Michou et al. (2017), has an average value of 27.5° C/km, therefore the calculated temperature at the bottom of the borehole is around 84 °C. Geothermal and lithostatic gradients are needed to calculate the seismic velocities at in situ conditions. Derivatives for pressure, measured from our experimental data were applied to calculated velocities at borehole conditions. Derivatives for temperature, available in the literature for limestone (Christensen 1985) and sandstone (Kern and Wenk 1990), are about 0.001 km s^{-1}°C^{-1}, therefore we considered that the effect of temperature is negligible in the range of temperatures of our borehole, and no correction for temperature was applied.

Velocity data measured during pressurization up to 250 MPa and depressurization cycles, were interpolated (solid line in Fig. 8) using the four-parameter equation of Wepfer and Christensen (1991) (Eq. 7). $V_{p,s}$ is the seismic velocity (m/s), P confining pressure (MPa), and A (m/s), a, B (m/s), and b (1/MPa) all are the four adjustable parameters.

$$V_{p,s}(P) = A\left(\frac{P}{100}\text{MPa}\right)^a + B\left(1 - e^{-bP}\right), \tag{7}$$

The equation was then used to calculate velocities at in situ conditions. The Wepfer and Christensen fitting

Table 4 Velocities (m/s) at borehole conditions

Sample		P_{conf} (MPa)	Compressional waves (m/s)						Shear waves (m/s)					
			V_p	A (m/s)	B (m/s)	a	b	$Z_p \times 10^7$	V_s	A (m/s)	B (m/s)	a	b	$Z_s \times 10^6$
HU01a	X	26	5459	5089	771	0	0.03	1.48	3037	2978	192	0.01	0.02	8.23
HU1b	Y		4826	4421	700	0.05	2.93	1.40	2714	2525	448	0.01	0.03	7.90
	Z		4907	4316	1078	0.01	0.04	1.33	2804	2757	249	0.01	0.02	7.60
HU03	X	26	4658	4186	892	0.03	0.04	1.26	2503	2309	548	0.01	0.02	6.80
	Y		NA	NA	NA	NA	NA	NA	NA	NA	NA	NA	NA	NA
	Z		4676	4323	743	0.01	0.03	1.27	2570	2414	448	0.01	0.02	6.99
HU06	X	26	4412	4059	790	0.01	0.03	1.22	2425	2337	393	0.02	0.02	6.70
	Y		4633	4348	679	0	0.02	1.33	2480	2219	608	0.01	0.02	7.53
	Z		4408	4015	797	0.03	0.04	1.20	2380	2163	604	0.01	0.02	6.46
HU07	X	48	5404	5123	829	0.01	0.01	1.47	2931	2646	547	0.01	0.02	7.95
	Y		5591	4860	997	0.07	0.07	1.51	3233	2981	349	0	0.03	8.43
	Z		5284	5003	760	0.01	0.01	1.43	3016	2932	173	0.01	0.02	8.18
HU09	X	49	4802	4647	829	0.06	0.01	1.31	2871	2643	484	0.01	0.01	7.81
	Y		4969	4940	550	0.05	0.01	1.45	2866	2639	469	0	0.01	8.07
	Z		4922	4443	1363	0.01	0.01	1.34	2870	2615	526	0	0.01	7.83
HU12	X	53	5168	4478	1697	0	0.01	1.40	3098	2910	476	0.01	0.01	8.38
	Y		5325	4659	1583	0	0.01	1.61	3086	2817	552	0	0.01	8.69
	Z		5234	4562	1724	0.01	0.01	1.42	3075	2804	557	0.01	0.01	8.34
HU13	X	55	4765	4702	410	0.02	0.01	1.26	2941	2882	252	0.01	0.01	7.78
	Y		NA	NA	NA	NA	NA	NA	NA	NA	NA	NA	NA	NA
	Z		4372	4094	834	0.02	0.01	1.17	2745	2670	263	0.01	0.01	7.33
HU14	X	61	5736	5696	686	0.01	0	1.54	3208	3196	57	0.01	0.01	8.59
	Y		5011	4421	700	0.05	2.93	1.60	3221	3207	143	0	0	8.60
	Z		5905	5782	312	0.01	0.01	1.59	3218	3216	56	0.01	0.01	8.65
BX107	X	74[a]	4179	3399	1413	0.01	0.01	1.19	2691	2117	678	0.04	0.03	7.64
	Z		5125	4210	1173	0.04	0.02	1.48	2890	2346	584	0.04	0.05	8.36
HU17	X	80	6158	6092	114	0.01	0.02	1.81	3397	3360	122	0	0	10.00
	Y		6608	6087	550	0.02	0.45	1.77	3707	3574	139	0	0.05	9.83
	Z		6157	6048	257	0.01	0.01	1.81	3440	3391	159	0	0	10.1
HU20	X	82	6707	5830	1161	0.01	0.02	1.91	3749	3649	140	0.02	0.02	10.7
	Y		6601	6349	527	0.04	0.01	1.92	3699	3306	511	0	0.02	10.6
	Z		6346	5557	1057	0.01	0.02	1.83	3670	3278	401	0	0.05	10.6
HU21	X	83	6062	5886	331	0	0.01	1.79	3300	3274	109	0	0	9.73
	Y		NA	NA	NA	NA	NA	NA	NA	NA	NA	NA	NA	NA
	Z		5673	5464	390	0.01	0.01	1.66	3268	3118	192	0	0.02	9.59
HU24	X	83	6781	6414	485	0.01	0.02	1.94	3676	3506	309	0	0.01	10.5
	Y		6258	5611	700	0.05	0.18	1.84	3541	3193	410	0	0.02	10.2
	Z		6473	5701	1009	0.01	0.02	1.88	3469	2987	500	0.03	0.1	10.1
HU25	X	77	5186	4716	841	0.01	0.01	1.39	3466	3100	555	0.01	0.01	9.30
	Y		5231	5018	505	0.03	0.01	1.42	3507	3227	523	0	0.01	9.44
	Z		5095	4376	1274	0.01	0.01	1.36	3493	3071	613	0.01	0.02	9.30
HU26	X	77	NA	NA	NA	NA	NA	NA	NA	NA	NA	NA	NA	NA
	Y		5374	4791	924	0.01	0.01	1.46	3401	3123	370	0.01	0.02	9.31
	Z		5471	5066	691	0	0.01	1.44	3659	3452	291	0.01	0.02	9.62
HU27	X	87	5484	4443	1394	0.01	0.02	1.52	3441	2832	682	0.02	0.03	9.54
	Y		5448	4536	1308	0.02	0.01	1.48	3360	2820	634	0.01	0.02	9.23
	Z		5503	3711	1949	0.03	0.03	1.53	3353	2790	600	0.02	0.03	9.32

Table 4 (continued)

Sample		P_{conf} (MPa)	Compressional waves (m/s)						Shear waves (m/s)					
			V_p	A (m/s)	B (m/s)	a	b	$\mathcal{Z}_p \times 10^7$	V_s	A (m/s)	B (m/s)	a	b	$\mathcal{Z}_s \times 10^6$
HU29	X	77	5670	5466	281	0.02	0.02	1.56	3350	3264	107	0.02	0.04	9.21
	Y		5440	4748	987	0.02	0.02	1.46	3407	3406	1827	0.01	0	8.82
	Z		5398	2339	3108	0.07	0.09	1.47	3214	3090	144	0.02	0.04	8.78

The in-situ confining pressure; (MPa) was derived using Equation (6) in text. *A*, *B*, *a*, and *b* are the parameters of the curve-fit of Wepfer and Christensen (1991) [Eq. (7) in text]. The acoustic impedance at borehole conditions (Pa s/m) for compressional- ($\mathcal{Z}_p$) and shear-waves ($\mathcal{Z}_s$) was calculated by the multiplication of seismic velocities and grain densities (Table 2)

NA Not available

a Lithostatic pressure for the sample BEX was considered as for a depth of 2630 m

parameters are presented in Table 4, together with the P- and S-wave velocities calculated for the lithostatic pressure conditions corresponding to the depth of the samples. Table NA presents also the seismic impedance ($\mathcal{Z}$), i.e. the product of velocity and density, calculated for each sample at in situ conditions. Dolomite from the Muschelkalk formation shows the highest values of impedance, and the lowest in the limestones of the Upper Jurassic series. The impedance was then used to calculate the reflection coefficients as explained in the following section.

4.6 Elastic moduli calculation

The relationship between the seismic velocities compressional- and shear-wave was used to calculate the Poisson ratio (Eq. 8), where *ver* means that we used velocities in the Z-direction while for *hor* we used velocity values either X- or Y-directions. As for anisotropy, the dynamic Poisson ratio shows considerable variations as a function of the confining pressure, especially in the low confining pressures range (< 150 MPa) until all microcracks have been completely closed. Within the mineral compressibility region, the Poisson ratio stabilizes and have a gentle slope (Fig. 9).

$$\nu_{\mathrm{hor,ver}} = \frac{1}{2}\frac{V_p^2 - 2V_s^2}{V_p^2 - V_s^2}, \tag{8}$$

The Poisson ratio, together with other elastic moduli that calculated along the horizontal and vertical directions for all the samples are as illustrated Fig. 11. All samples tend to concentrate along the 1:1 line, as expected in isotropic rocks. The only exception is sample BX-107 reflecting the anisotropic character of this sample. In Fig. 11 it is visible that dolomite-dominant Muschelkalk samples have higher Young and Bulk moduli compared to the calcite dominant carbonates of Jurassic age, while for Shear modulus the distinction is less clear.

5 Discussion

5.1 Influence of porosity on velocities

The observation on texture and mineral content at the plug-scale provides useful information for better understanding the seismic characteristics of the studied rock types. In Fig. 12 the average seismic velocities calculated at 40 MPa confining pressure are plotted against effective porosity (a) and average permeability (b). We chose 40 MPa as a reference pressure for those diagrams in order to consider the effect of partially open fractures at an average in situ pressure condition.

The correlation between porosity and permeability is positive (Fig. 12b), as expected by a general common behavior. The only sample that significantly deviates from the regression line is HU07, a limestone from the middle Jurassic section, that shows a low permeability/porosity ratio. It has to be noted that the permeability of the sample is strongly anisotropic, with *k* values measured within the bedding plane three orders of magnitude higher than the one measured perpendicular to the bedding. The effect of the extremely low permeability in the vertical direction reduces the average permeability and is responsible for the deviation of the sample from the general trend.

Regarding the link between velocities and porosity, even if a negative trend is recognizable, the scatter of the data is quite large, meaning that for rocks of similar porosity we can have very different P and S velocities. Looking at closer detail we notice that for limestones, the monomineralic Upper Jurassic samples show a linear negative correlation between porosity and both P- and S-waves velocities. The same is observed in the argillaceous limestones of Middle and Lower Jurassic age, but with a steeper negative correlation, indicating that the decrease of velocity with increasing porosity is enhanced by other factors, probably associated with the effects of mineralogical composition. On the contrary in the Muschelkalk Formation, the porosity/

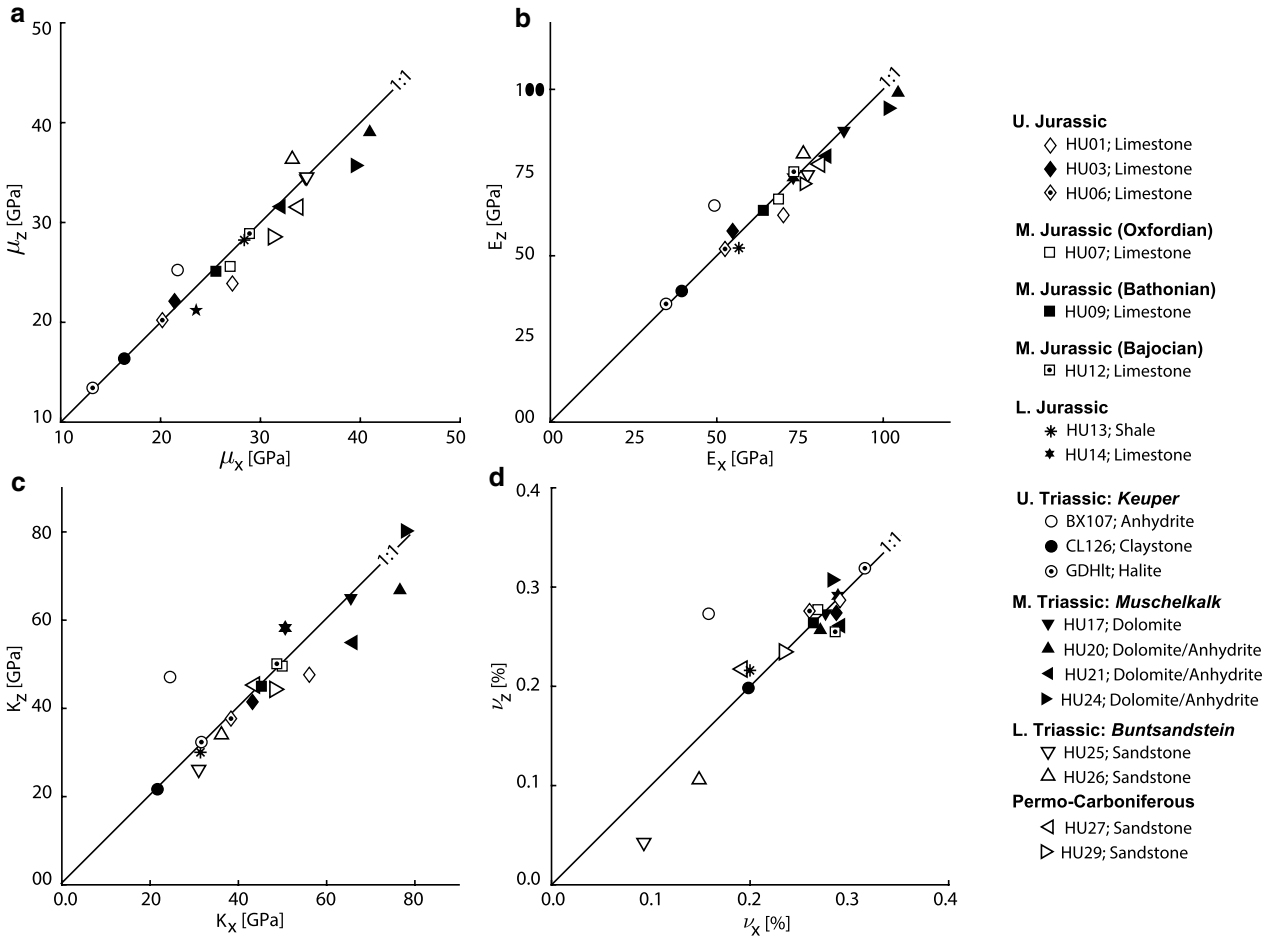

Fig. 11 Cross-plots for the studied plugs of **a** horizontal and vertical shear Modulus (μ), **b** horizontal and vertical Young modulus (E), **c** horizontal and vertical Bulk Modulus (K), and **d** horizontal and vertical Poisson's ratio (ν)

velocity trend is positive indicating that porosity has a little influence on seismic properties, and other factors are more relevant. For sandstones, again the correlation is quite complex: the velocities nicely follow the general decreasing trend, for compressional-wave, but not for shear-wave.

In summary, the seismic velocities and elastic properties depend not only on porosity as it is evident within the large scatter-type of data for the velocity-porosity relationships. The constituent minerals have a major contribution for those variations, together with other factors that are only partially addressed in this work such as cementation, pore geometry, and grain size.

5.2 Influence of mineral contents on velocities

The modal composition obtained from QEMSCAN analysis was used to interpret the influence of the main mineral components on the seismic properties of the rocks. The average of the seismic velocities recalculated at room pressure conditions (V_{p0} and V_{s0}) are plotted against the main rock forming minerals of the studied samples and shown in Fig. 13. We choose to plot V_{p0} and V_{s0} against modal components fractions, because they represent the intrinsic seismic properties i.e. the elastic properties related to the mineral skeleton and not to the void space (pores, fractures).

The Permo-Carboniferous-Lower Triassic sandstones are primarily composed of quartz (39–86%). A variable amount of clay minerals (3–19% of illite and kaolinite), is present either along the grain boundaries, in the occluded pores (sample HU25, Fig. 6e) or as multiple thinly laminated layering of fine-grained bands (HU29, Fig. 6f). Even small amounts of clay can significantly change the elastic properties of the sandstone (Castagna et al. 1985; Han et al. 1986; Klimentos 1991). In fact, the average V_p of quartz (Table 5) is generally higher than the average V_p of illite or kaolinite, even if for the latter data reported in literature span over quite a large range (Mondol et al. 2008,

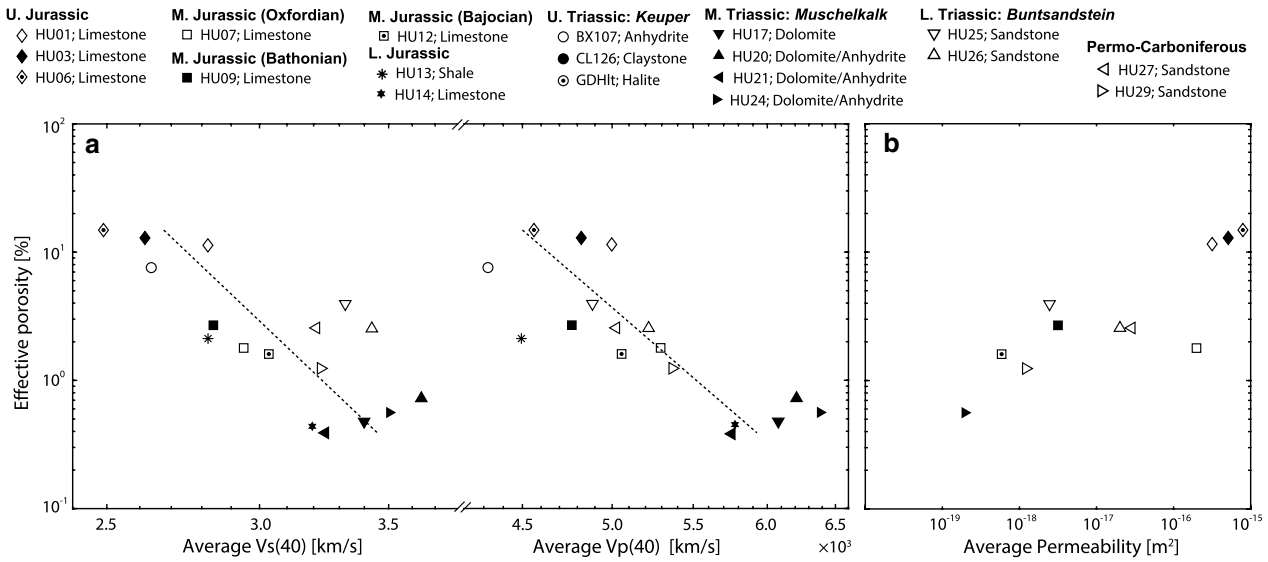

Fig. 12 Cross-plot is showing the relationship between the average seismic velocity and the effective porosity. The values of the seismic velocities were calculated at 40 MPa confining pressure using the empirical formula of Wepfer and Christensen (1991). A clear negative trend confirms the general observation that the seismic velocity decreases with increasing effective porosity. The significant dispersion in the velocity-porosity relationship, particularly for the shear velocity, can be related to other controlling factors such as the mineralogy, grain size, grain shape and pore geometry. Error bars are within symbols

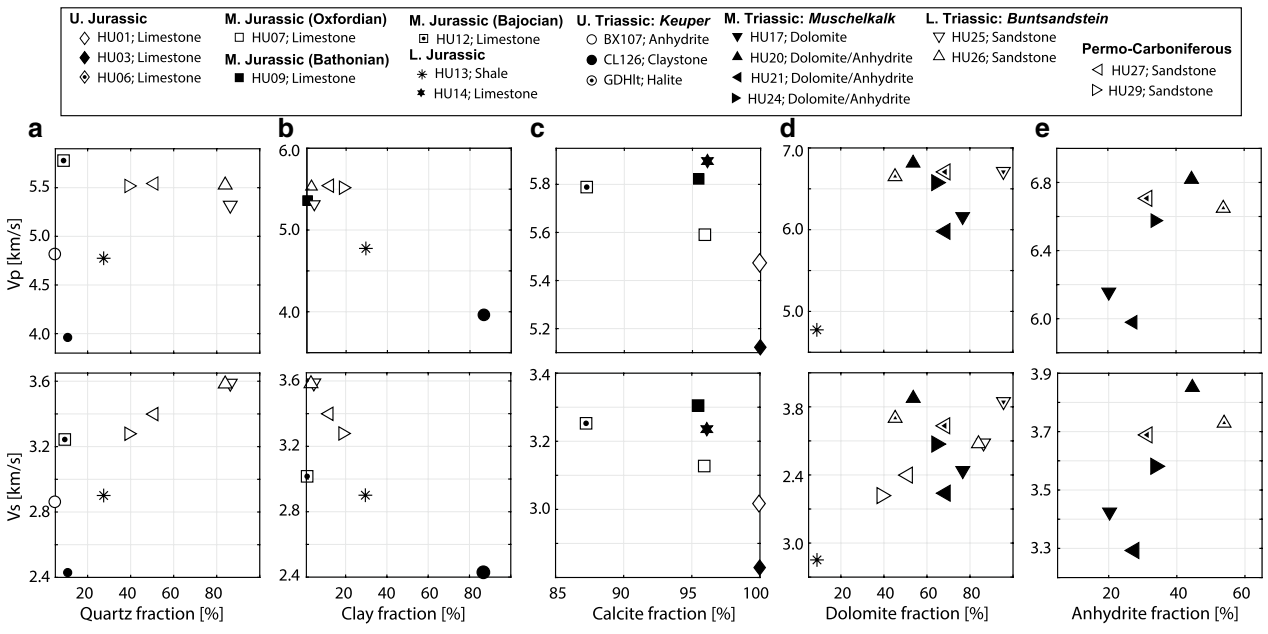

Fig. 13 Average seismic velocity of compressional and shear-waves are plotted against the content of various rock-forming minerals. It shows that the compressional velocities decrease with increasing quartz and clay content, while for shear waves the correlation is opposite for quartz (decrease) than for clay (increase). Despite a certain dispersion of the data, that we interpret as due to factors such as alterations and diagenesis, we observe a positive correlation between velocities (P- and S-waves) and dolomite content. Less evident is the correlation of velocities with calcite content and with evaporitic minerals. Error bars are within symbols

Table 5 Elastic properties of some commons rock-forming minerals

Minerals	Bulk M. (GPa)	Shear M. (GPa)	Density (g/cm^3)	Vp (km/s)	Vs (km/s)	Poisson Ratio (–)	References
Framework silicates							
K-feldspar	62.66	31.85	2.56	6.41	3.53	0.28	Hearmon (1984)
Quartz	37	44	2.65	6.05	4.09	0.08	Carmichael (1990)
	36.5	45.6	2.65	6.06	4.15	0.06	Anderson and Liebermann (1966)
	37.9	44.3	2.65	6.05	4.09	0.08	McSkimin et al. (1965)
Plagioclase	75.6	25.6	2.63	6.46	3.12	0.35	Woeber et al. (1963)
Sheet silicates							
Muscovite	61.5	41.1	2.79	6.46	3.84	0.23	Aleksandrov and Ryzhova (1961)
	42.9	22.2	2.79	5.10	2.82	0.28	Ellis et al. (1988)
Biotite	59.7	42.3	3.05	6.17	3.73	0.21	Aleksandrov and Ryzhova (1961)
	41.1	12.4	3.05	4.35	2.02	0.36	Ellis et al. (1988)
Clay minerals							
Illite	52.59	31.69	2.79	5.83	3.37	0.25	Katahara (1996)
	NP	NP	NP	4.32	2.54	0.24	Eastwood et al. (1987)
Kaolinite	55	31.8	2.52	6.23	3.55	0.26	Katahara (1996)
	1.5	1.4	1.58	1.44	0.93	0.14	Woeber et al. (1963)
Gulf clays	25	9	2.55	3.81	1.88	0.34	Han et al. (1986)
	21	7	2.6	3.41	1.64	0.35	Tosaya (1983)
Sulfates							
Anhydrite	56.1	29.1	2.98	5.64	3.13	0.28	Schwerdtner et al. (1965)
	62.1	33.6	2.96	6.01	3.37	0.27	Rafavich et al. (1984)
Carbonates							
Siderite	123.7	51.0	3.96	6.96	3.59	0.32	Christensen (1972)
Calcite	76.8	32.0	2.71	6.64	3.44	0.32	Simmons (1965)
	63.7	31.7	2.70	6.26	3.42	0.29	Bhimasenachar (1945)
	70.2	29.0	2.71	6.34	3.27	0.32	Peselnick and Robie (1962)
	74.8	30.6	2.71	6.53	3.36	0.32	Dandekar (1968)
	68.3	28.4	2.71	6.26	3.24	0.32	Anderson and Liebermann (1966)
Dolomite	94.9	45	2.87	7.34	3.96	0.30	Humbert and Plicque (1972)
	76.4	49.7	2.87	7.05	4.16	0.23	Nur and Simmons (1969)
Halite	24.8	14.9	2.16	4.55	2.63	0.25	Simmons (1965)

NP Not provided

and references therein). Similarly, averaged V_s are much lower in clay minerals than in quartz. Therefore, the presence of clay in sandstone has the effect to lower both velocities, with greater effect on shear component. The increase in V_p and decrease in V_s within Bundsandstein samples (HU25 and HU27) is attributed to the decreasing percentage of quartz, as shown in Fig. 13a. Siderite (not shown in Fig. 13) is another mineral phase present in the Permo-Carboniferous sandstones (samples HU27 and HU29) with concentrations similar to those in clay minerals. The elastic moduli of siderite are much higher than the moduli of clay and quartz, therefore the presence of siderite has the effect to increase the elastic moduli, and consequently V_p and V_s of the whole rock. Siderite and clay in the sandstones have then competing effects.

The effect of clay in reducing both V_p and V_s is also visible in the shale (HU13, 30% illite) and in the claystone (CL126; 87% illite + kaolinite); Fig. 13b. The anisotropy of the only shale in our collection is relatively low ($AV_p = 4.16\%$, and $AV_s = 5.80\%$) compared with data in literature (e.g. in Valcke et al. 2006), probably due to the scarce iso-orientation of the grains and to the competing effect of quartz and calcite; Fig. 6a.

There is not a clear influence of calcite on the velocity of the limestones in our collection (Fig. 13c). The same is observed for the dolomite (Fig. 13d), even if a slight tendency towards increased velocities is observed especially within the sandstones. The positive correlation with velocity is more marked for anhydrites in the

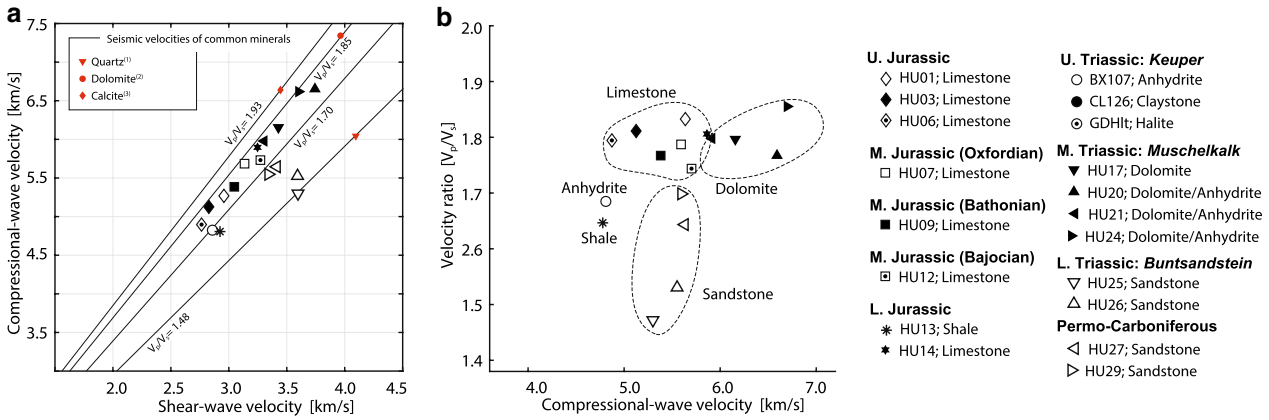

Fig. 14 A cross-plot of average compressional- versus average shear-wave velocities with isolines for Vp/Vs ratio of different common minerals. The compressional and shear wave velocities for such minerals were after (1) Carmichael (1990), (2) Humbert and Plicque (1972), (3) Chen et al. (2001). (B) Clusters of rock-types based on the plotting of the seismic velocity ratio vs. the compressional-wave velocity. Similar clustering pattern was found for shear-wave velocity. Error bars are within symbols

Muschelkalk formation (Fig. 13e): the higher the anhydrite content, the higher V_p and V_s.

The influence of mineral content for both V_p and V_s is not evident, V_p anisotropy tends to be higher in carbonates (high calcite content) than in sandstones (high quartz content), but it clearly does not depend on whether the rock is clastic or carbonates but seems to rely on the nature of the heterogeneities and microtexture within the rock (i.e., clay banding, laminations, microcracks, etc.). The influence of mineral content on V_p/V_s ratio is summarized in Fig. 14a, where shear- vs. compressional-wave of our samples are plotted together with the seismic velocities values for single crystals of quartz, calcite, and dolomite, i.e. the main components of our rocks.

The sandstones fall either on the line of constant V_p/V_s ratio of quartz, or in an intermediate region between the lines of quartz and clay minerals, nicely following the progressive content of clay minerals from top to bottom of the section. The Muschelkalk samples fall in the narrow field between lines of constant V_p/V_s anhydrite and dolomite. The Dogger limestones fall together with the Upper Jurassic limestone, all below the line V_p/V_s for calcite. This result is interpreted for Upper Jurassic limestone as the effect of porosity, lowering more the shear- than the compressional-wave (Toksöz et al. 1976), and for Dogger limestones as the effect of quartz content.

A summary of single crystal elastic properties of the main minerals, averaged along all propagation directions, is reported in Table 5. as a reference for the considerations described below.

6 Seismic reflectivity

The seismic impedance ($\mathcal{Z}$) of an elastic medium controls the seismic reflection process because seismic energy can be reflected at interfaces only where there is a change in impedance across the interface. It is defined as the product of velocity and density. The Reflection Coefficient (R_c) is the difference in seismic impedance over the sum of seismic impedance of two rock types; Eq. (9).

$$\begin{aligned} R_c &= \frac{\mathcal{Z}_2 - \mathcal{Z}_1}{\mathcal{Z}_2 + \mathcal{Z}_1}, \\ &= \frac{\rho_2 V_2 - \rho_1 V_1}{\rho_2 V_2 + \rho_1 V_1}, \end{aligned} \tag{9}$$

R_c will be then a positive number when $V_2 > V_1$, and a negative number when $V_2 < V_1$, which means equal or inverse polarity between incident and reflected waves, respectively. The larger the contrast in seismic impedance, the larger the amount of incident energy that is reflected (and the smaller the amount that is transmitted). The seismic impedance at the interface of different rock-types, calculated from intrinsic velocity as well as at its corresponding borehole conditions, is provided in Table 6. We tested R_c of the interfaces that occur repeatedly in the sequence crosscut by the Humilly borehole. We could not retrieve samples from each interface (above and below interfaces), as big part of the sequence was not sampled, but we tried to sample each litho-type and combine them in order to simulate most of the interfaces that occur at Humilly. That is why we also inserted data from

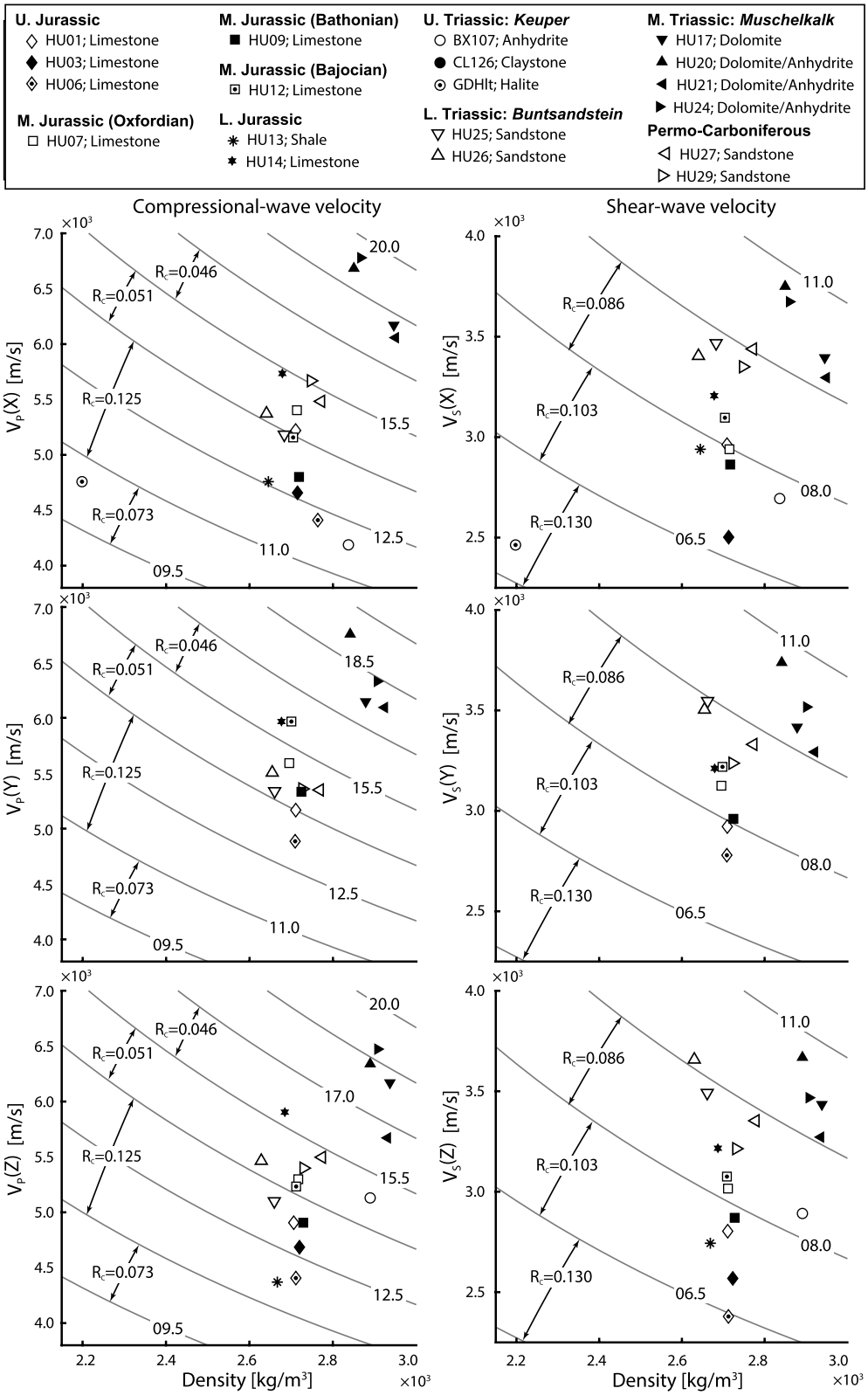

Fig. 15 Grain density versus the compressional and shear seismic velocity with lines of constant acoustic impedance. Reflection coefficients values are reported between the acoustic impedance contours. All seismic velocities have been calculated at borehole conditions. Error bars are within symbols

Table 6 Seismic Impedance (Pa s/m) for compressional-waves propagating perpendicular to the bedding planes of the sedimentary formations (plugs in Z-direction)

Core	Sample	Depth (m)	Rock-type (age)	Seismic Impedance ($\times 10^7$ Pa s/m)	
				Z_0	Z_{BHP}
Core I	HU01	1015.0	Limestone (Upper Jurassic)	1.47	1.33
	HU03	1018.1		1.93	1.28
	HU06	1020.1		1.32	1.20
Core II	HU07	1853.4	Argillaceous limestone (Middle Jurassic)	1.51	1.44
	HU09	1860.8		1.46	1.34
	HU12	2003.5		1.55	1.42
Core III	HU13	2242.7	Shale (Liassic)	1.25	1.17
	HU14	2468.3	Limestone (Lower Jurassic)	1.61	1.59
Core IV	BX107	2630.0	Anhydrite-Claystone-Halite (Upper Triassic)	1.23	1.45
	CL126	2710.0		1.10	1.11
	GDHlt	2770.0		1.05	1.02
Core V	HU17	2905.5	Dolomite Anhydrite (Middle Triassic)	1.81	1.81
	HU20	2922.5		1.85	1.84
	HU21	2930.3		1.69	1.66
	HU24	2967.0		1.93	1.89
	HU25	3028.3	Sandstone (Lower Triassic)	1.42	1.36
	HU26	3030.2		1.46	1.44
	HU27	3037.5	Sandstone (Permo-Carboniferous)	1.55	1.52
	HU29	3038.8		1.50	1.48

Seismic Impedance is calculated as a function of intrinsic seismic velocities, Z_0, as well as at the Bottomhole Pressure, Z_{BHP}. The in-situ seismic velocity was derived following Wepfer and Christensen (1991) relationship (Eq. 7) in text and using the parameters *A*, *B*, *a*, and *b* provided in Table 4)

literature for clays and evaporates because they were not sampled in Humilly. For the seismic wave to be reflected at normal incidence angle, the interface between two different rock types must generate a significant impedance contrasts and have a minimum width equal to one-quarter of seismic wavelength (Christensen 1989; Nanda 2016; Warner 1990). According to Sheriff and Geldart (1995), an $R_c = 0.1$ represents a strong reflector, whereas good reflections originate from rock interfaces with $R_c \geq 0.04$.

In Figure 15, the compressional- and shear-wave velocities of the samples at borehole conditions have been plotted against the grain density. In order to investigate the effect of the seismic anisotropy on the acoustic impedance, and therefore on reflection coefficient, the velocities measured along the three structural directions have been used. Isolines of acoustic impedance (Pa s/m^3) have been drawn on the plots and the reflection coefficient arising from adjacent impedance isolines is indicated.

Rock-types plotting at a distance greater than two isolines are considered as a potential reflector. Figure 15 shows that the dolomite-rich Muschelkalk plots in the fast $V_{p,s}$ and higher density corner (upper right) referring to high acoustic impedance compared to the halite sample of Keuper which plot in the lower left corner of the figure. The stratigraphic interface between the Muschelkalk and the overlying Keuper Halite, therefore, gives a strong reflection.

The measurements along the Z-direction were used to simulate the normal incidence of seismic waves encountering the sub-horizontal layering during a near-vertical incidence reflection survey. The strongest reflecting interfaces were found within the evaporitic facies of the Keuper (Lettenkohle) between the overlying Liassic carbonates and underlying Muschelkalk

(See figure on next page.)

Fig. 16 Comparison between grain density, seismic velocities and impedance measured in the laboratory with corresponding physical parameters from borehole logging. Compressional velocities along horizontal (red square) and vertical (blue circle) plugs have been calculated at in-situ condition applying the velocity/pressure derivatives using empirical formula of Wepfer and Christensen (1991). The vertical acoustic impedance has been used to calculate the reflection coefficient to simulate the normal incidence of seismic waves. Error bars are within symbols. Samples of Core IV are after: **a** Müller and Briegel (1977), **b** Freund (1992), **c** Yan et al. (2016)

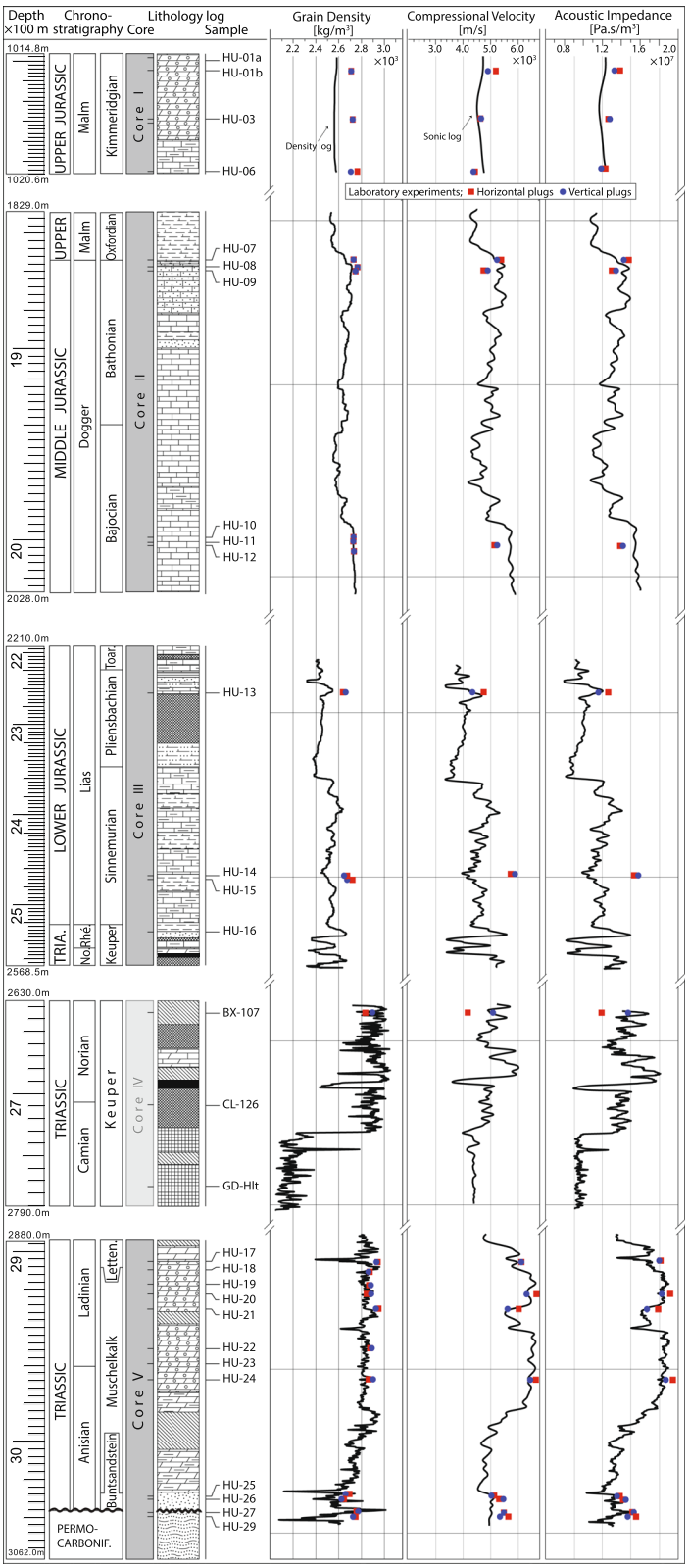
Depth ×100 m
Chrono-stratigraphy
Core
Lithology log
Sample
Grain Density [kg/m³]
Compressional Velocity [m/s]
Acoustic Impedance [Pa.s/m³]
Density log
Sonic log
Laboratory experiments; Horizontal plugs Vertical plugs
UPPER JURASSIC
Malm
Kimmeridgian
Core I
HU-01a
HU-01b
HU-03
HU-06
MIDDLE JURASSIC
Dogger
Oxfordian
Bathonian
Bajocian
Core II
HU-07
HU-08
HU-09
HU-10
HU-11
HU-12
LOWER JURASSIC
Lias
Pliensbachian
Toar
Sinnemurian
Core III
HU-13
HU-14
HU-15
HU-16
TRIA.
Rhé
Keuper
TRIASSIC
Norian
Camian
Keuper
Core IV
BX-107
CL-126
GD-Hlt
Ladinian
Anisian
Muschelkalk
Letten
Buntsandstein
Core V
HU-17
HU-18
HU-19
HU-20
HU-21
HU-22
HU-23
HU-24
HU-25
HU-26
HU-27
HU-29
PERMO-CARBONIF.

unit (R_c= 0.27) and between the Dogger and the Upper Jurassic carbonates (R_c= 0.09). Reflective interfaces could exist between Keuper and Sinemurian carbonates.

Figure 16 shows a comparison between density, seismic velocities, and acoustic impedance measured in laboratory and the logging data. For grain density, the results of the laboratory measurements are significantly higher only in the Upper Jurassic carbonates, reflecting the role of the high porosity in that section. Velocities are only slightly higher for sample HU01. Slightly higher values have been measured also in the limestones of the lower Jurassic section both for density and velocities, a difference that could also arise from the used resonance frequency (1 MHz transducers in Laboratory, and 10 kHz for acoustic log).

7 Conclusions

We have presented new experimental data on seismic properties using a collection of cylindrical samples obtained from the Humilly-2 borehole (France), which reached a depth of 3051 m in the top of Permo-Carboniferous sediments. Experimental measurements of physical rock properties and mineralogical analysis were performed to explore the links between sedimentary facies and seismic characteristics and provide a tool in the interpretation of seismic field data in terms of geological formations.

Among the studied formations, grain densities (kg m^{-3}) measured at ambient conditions show a wide range from 2200 to 2935. Seismic velocities (m s^{-1}) at the atmospheric pressure are in the range 3955 to 6648 and 2426 to 3737 for P- and S-wave propagation modes, respectively. The seismic anisotropy seems to be quite low ($AV_{p,s}$= 0.3–6%) in the limestone of Jurassic age, Muschelkalk, Sandstone (Triassic and Permo-Carboniferous), and Liassic Shale, while anhydrite exhibits an unusually high anisotropy value (AV_p= 20%, AV_s= 7%). The variations in seismic characteristics are due to mineral content, porosity and micro-textural features.

In the Upper Jurassic limestone, monomineralic and highly porous limestones, the seismic behaviors are linked to porosity, that varies in volume and size over several orders of magnitude. These rocks are almost isotropic, in a good agreement with the homogeneity of the samples (absence of bedding, compositional layering, and shape preferred orientation of grains) observed both at hand-specimen scale and in thin section. The various generations of calcite, either primary or diagenetic, presumably have no optical preferred orientation. Limestones with the same characteristics as the Upper Jurassic section might generate good reflectors if in contact with dolomitic/anhydrite rocks such as the Muschelkalk formation. Also, the stratigraphic contact between Upper Jurassic limestone and underlying Dogger would give rise to a fairly high reflection.

In the Dogger limestones, the compressional- and shear-wave velocities are on average slightly higher than in Upper Jurassic limestone carbonates, as an effect of the low porosity. The mineral composition of these carbonates is more complex than in the Upper Jurassic limestones: clay minerals, dolomite and quartz are present and might be the reason of a V_p/V_s ratio slightly lower than for calcite single crystals. Their impedance might give rise to a reflective contact with the dolomitic Muschelkalk or with a shale such as the Liassic shale unit.

The only shale in our collection, in the Liassic shale unit, shows one of the lowermost values for compressional-wave velocity, in agreement with the relatively high content of clay minerals. The low V_p/V_s ratio can be influenced by the presence of quartz. The anisotropy, due to iso-orientation of phyllosilicate, is probably lowered by contrasting effects of quartz grains with no optical preferred orientation. The shale might produce good reflectors if in contact with sandstones, or dolomitic carbonates, and also with some limestones. The Liassic shale unit would give rise to a good reflection at the stratigraphic contact with the underlying Liassic carbonates.

The highest values of the seismic velocity and density were measured in the Muschelkalk; therefore, those rocks might give rise to good reflectors if in contact with almost all the other lithotypes. That Muschelkalk anhydrite/dolomite interface produces high-energy seismic reflections has been known since decades. What's new in our work is that we've data from real rock samples that justify these observations from seismic logs. The high velocities might be related to the high content of dolomite, a mineral with relatively high velocity compared to other common components such as calcite or quartz. The V_p/V_s ratio is also similar to the one reported for dolomite single crystal. The Muschelkalk anisotropy is relatively high (> 5%), due to the small-scale compositional layering, visible at hand specimen and thin section scale.

The sandstones of the Lower Triassic and Permo-Carboniferous section present a quite wide range of V_p and V_s values, that can be correlated with the volume of dolomite and siderite in the rocks, contributing to increase the velocities. The V_p/V_s ratio is also different from the pure quartz value in samples with more complex modal composition. The highest anisotropy values have been reached on the only sample with high content of clay minerals, distributed in thin layers.

The comparison of lab data and log data show a relatively good agreement, with exception for density in those rocks with high porosity. The lab measurements, performed at dry conditions, slightly underestimate the

log values for bulk density and overestimate it for grain density, an effect that can be clearly explained by the presence of filled pores in the in-situ measurements.

The reflection coefficients calculated for the stratigraphic sequence in Humilly show possible good reflectors at the top of the Muschelkalk and at the top of the Keuper (with the caveat that we used samples from different boreholes or literature due to absence of Keuper samples in Humilly borehole). A good reflector can also exist at the contact between the Buntsandstein and Muschelkalk units.

Acknowledgements
The Swiss Commission for Geophysics (SGPK) has supported the collection of physical parameters through the SAPHYR project. The authors are grateful to Structural Geology and Tectonics group of ETH Zurich under Prof Jean-Pierre Burg leadership for financing subsurface dataset needed to complete this work. Mahmoud Hefny acknowledges the doctoral fellowship at ETH Zurich provided by the Swiss Government Excellence Scholarship (no. 2015.0718). The authors are highly indebted to Rock Physics and Mechanics Laboratory of ETH Zurich for the support in measuring the rock physics properties of the selected core samples. Quinn C. Wenning, Claudio Madonna, Aymeric Le Cotonnec, and Elme Rusillon are thanked for their discussion and assistance during the preparation of this study. The author are grateful to the two anonymous reviewers, for their constructive comments that improved the manuscript.

Authors' contributions
MH conducted the experiments, analysed the data, prepared figures and wrote the main manuscript. AZ supervised the whole work and wrote the main manuscript. YM was responsible for petrographic characterization. AdH performed QEMSCAN experiment and conducted data processing. AM designed the research work. All authors reviewed the manuscript. All authors read and approved the final manuscript.

Availability of data and materials
Supporting dataset accompanies this paper including the experimental raw data is publicly accessible through a GFZ data service repository (Hefny et al. 2020). URL: https://doi.org/10.5880/fidgeo.2020.029.

Competing interests
The authors declare that they have no competing interests.

Author details
[1] Geothermal Energy and Geofluids, Institute of Geophysics, ETH Zurich, 8092 Zurich, Switzerland. [2] Geology Department, South Valley University, Qena 83523, Egypt. [3] Swiss Seismological Service, ETH Zürich, 8092 Zurich, Switzerland. [4] Department of Mechanical and Process Engineering, ETH Zürich, 8092 Zürich, Switzerland. [5] Department of Earth Sciences, University of Geneva, 1205 Geneva, Switzerland.

Received: 19 March 2020 Accepted: 16 June 2020
Published online: 13 July 2020

References

Aleksandrov, K., & Ryzhova, T. (1961). The elastic properties of rock forming minerals II: Layered silicates. *Bulletin USSR Academy of Science, Geophysics Series*, *9*, 1165–1168.

Almqvist, B. S. G., Hirt, A. M., Herwegh, M., Ebert, A., Walter, J. M., Leiss, B., et al. (2013). Seismic anisotropy in the Morcles nappe shear zone: Implications for seismic imaging of crustal scale shear zones. *Tectonophysics*, *603*, 162–178.

Anderson, O. L., & Liebermann, R. C. (1966). Sound velocities in rocks and minerals. Report, VESIAC State-of-the-Art Report No. 7885–4-x, University of Michigan.

Barberini, V., Burlini, L., & Zappone, A. (2007). Elastic properties, fabric and seismic anisotropy of amphibolites and their contribution to the lower crust reflectivity. *Tectonophysics*, *445*(3–4), 227–244.

Becker, D., Rauber, G., & Scherler, L. (2013). New small mammal fauna of late Middle Eocene age from a fissure filling at La Verrerie de Roches (Jura, NW Switzerland). *Revue de paléobiologie*, *32*(2), 433–446.

Bhimasenachar, J. (1945). Elastic constants of calcite and sodium nitrate. In *Proceedings of the Indian Academy of Sciences-Section A*, vol. 22, pp. 199. Berlin: Springer.

Birch, F. (1960). The velocity of compressional waves in rocks to 10 kilobars, Part 1. *Journal of Geophysical Research*, *65*(4), 1083–1102.

Birch, F. (1961). The velocity of compressional waves in rocks to 10 kilobars, Part 2. *Journal of Geophysical Research*, *66*(7), 2199–2224.

Brace, W. F., Walsh, J. B., & Frangos, W. T. (1968). Permeability of granite under high pressure. *Journal of Geophysical Research*, *73*(6), 2225–2236.

Brentini, M. (2018). *Impact d'une donnée géologique hétérogène dans la gestion des géo-ressources: analyse intégrée et valorisation de la stratigraphie à travers le bassin genevois (Suisse, France)*. Department of Earth Sciences: Thesis.

Brown, L. D. (1986). Aspects of COCORP deep seismic profiling. *Reflection seismology: A global perspective* (p. 13). Washington, D.C.: American Geophysical Union.

Burke, M. M., & Fountain, D. M. (1990). Seismic properties of rocks from an exposure of extended continental crust-new laboratory measurements from the Ivrea Zone. *Tectonophysics*, *182*(1–2), 119–146.

Carmichael, R. S. (1990). *Practical handbook of physical properties of rocks and minerals. Physical properties of rocks and minerals*. Boca Raton: CRC Press.

Castagna, J. P., Batzle, M. L., & Eastwood, R. L. (1985). Relationships between compressional-wave and shear-wave velocities in clastic silicate rocks. *Geophysics*, *50*(4), 571–581.

Charollais, J., Clavel, B., Granier, B., Busnardo, R., & Conrad, M. A. (2013). Discussion of the paper by godet et al. 2011, entitled "reconciling strontium-isotope and k–ar ages with biostratigraphy: the case of the Urgonian platform, early cretaceous of the Jura mountains, Western Switzerland"(swiss journal of geosciences, 104, 147–160). *Swiss Journal of Geosciences*, 106(3):559–567.

Charollais, J.-J., Weidmann, M., Berger, J.-P., Engesser, B., Hotellier, J.-F., Gorin, G. E., et al. (2007). La molasse du bassin franco-genevois et son substratum. *Archives des Sciences*, *60*, 59–174.

Chelle-Michou, C., Do Couto, D., Moscariello, A., Renard, P., & Rusillon, E. (2017). Geothermal state of the deep Western Alpine Molasse Basin, France-Switzerland. *Geothermics*, *67*, 48–65.

Chen, C.-C., Lin, C.-C., Liu, L.-G., Sinogeikin, S. V., & Bass, J. D. (2001). Elasticity of single-crystal calcite and rhodochrosite by Brillouin spectroscopy. *American Mineralogist*, *86*(11–12), 1525–1529.

Christensen, N. I. (1972). Elastic properties of polycrystalline magnesium, iron, and manganese carbonates to 10 kilobars. *Journal of Geophysical Research*, *77*(2), 369–372.

Christensen, N. I. (1985). *Measurements of dynamic properties of rock at elevated temperatures and pressures*. American Society for Testing and Materials, Philadelphia, ASTM International STP 869, pp. 93–107.

Christensen, N. I. (1989). Reflectivity and seismic properties of the deep continental crust. *Journal of Geophysical Research: Solid Earth and Planets*, *94*(B12), 17793–17804.

Claerbout, J. F. (1985). *Imaging the earth's interior*. Oxford: Blackwell Science Inc, Blackwell Scientific Publications.

Clerc, N., Rusillon, E., Moscariello, A., Renard, P., Paolacci, S., & Meyer, M. (2015). Detailed structural and reservoir rock typing characterisation of the Greater Geneva Basin, Switzerland, for geothermal resource assessment. *Proceeding of the World Geothermal Congress 2015, Melbourne, Australia*, pp. 10.

Dandekar, D. P. (1968). Pressure dependence of the elastic constants of calcite. *Physical Review*, *172*(3), 873.

Debelmas, J., Michel, R., & MILLOT, G. (1961). Silicifications par altération climatique dans les séries alpines. *Travaux du Laboratoire de Géologie de la Faculté des Sciences de Grenoble*, *37*, 7–14.

Dickson, J. A. D. (1965). A modified staining technique for carbonates in thin section. *Nature*, *205*(4971), 587.

Diepolder, G. W., Allenbach, R., Baumberger, R., et al. (2015). GeoMol—assessing subsurface potentials of the Alpine Foreland Basins for sustainable planning and use of natural resources–Project Report. Report.

Disler, C. (1914). *Stratigraphie und Tektonik des Rotliegenden und der Trias beiderseits des Rheins zwischen Rheinfelden und Augst*. E. Birkhäuser.
Eastwood, R., Castagna, J., Justice, M., McCormack, M., Lee, S., Suyama, K., Imai, T., Ohtomo, H., Ohta, K., Takahashi, T., Fix, J., Robertson, J., & Pritchett, W. (1987). *4. Exploration Applications*, pp. 139–196. Geophysical Developments Series. Society of Exploration Geophysicists.
Ellis, D., Howard, J., Flaum, C., McKeon, D., Scott, H., Serra, O., et al. (1988). Mineral logging parameters: Nuclear and acoustic. *The Technical Review*, *36*(1), 38–38.
Freund, D. (1992). Ultrasonic compressional and shear velocities in dry clastic rocks as a function of porosity, clay content, and confining pressure. *Geophysical Journal International*, *108*(1), 125–135.
Gassmann, J., Gysel, M., & Schneider, J. F. (1979). *Anhydrit als Wirtgestein für die Endlagerung radioaktiver Abfälle in der Schweiz*. Nationale Genossenschaft für die Lagerung Radioaktiver Abfälle.
Gorin, G. E., Signer, C., & Amberger, G. (1993). Structural configuration of the western Swiss Molasse Basin as defined by reflection seismic data. *Eclogae Geologicae Helvetiae*, *86*(3), 693–716.
Gottlieb, P., Wilkie, G., Sutherland, D., Ho-Tun, E., Suthers, S., Perera, K., et al. (2000). Using quantitative electron microscopy for process mineralogy applications. *Journal of Minerals, Metals and Materials Society*, *52*(4), 24–25.
Grab, M., Zürcher, B., Maurer, H., & Greenhalgh, S. (2015). Seismic velocity structure of a fossilized Icelandic geothermal system: A combined laboratory and field study. *Geothermics*, *57*(Supplement C), 84–94.
Han, D., Nur, A., & Morgan, D. (1986). Effects of porosity and clay content on wave velocities in sandstones. *Geophysics*, *51*(11), 2093–2107.
Hearmon, R. (1984). The elastic constants of crystals and other anisotropic materials. *Landolt-Börnstein Tables*, *3*(18), 559.
Hefny, M., Zappone, A., Makhloufi, Y., de Haller, A., & Moscariello, A. (2020). Experimental rock physics for the calibration of seismic-data interpretation: The case of the borehole Humilly-2 (France) in the Geneva area. *GFZ Data Services*,. https://doi.org/10.5880/fidgeo.2020.029.
Humbert, P., & Plicque, F. (1972). Propriétés élastiques de carbonates rhomboédriques monocristallins: calcite, magnésite, dolomite. *CR Academy Science Paris*, *275*, 291–304.
Jenny, J., Burri, J.-P., Muralt, R., Pugin, A., Schegg, R., Ungemach, P., et al. (1995). Le forage géothermique de Thônex (Canton de Genève): Aspects stratigraphiques, tectoniques, diagénétiques, géophysiques et hydrogéologiques. *Eclogae Geologicae Helvetiae*, *88*(2), 365–396.
Jones, S. C. (1972). A rapid accurate unsteady-state Klinkenberg permeameter. *Society of Petroleum Engineers Journal*, *12*(05), 383–397.
Katahara, K. W. (1996). Clay mineral elastic properties. In *1996 SEG Annual Meeting*. Society of Exploration Geophysicists.
Kern, H., & Wenk, H.-R. (1990). Fabric-related velocity anisotropy and shear wave splitting in rocks from the santa rosa mylonite zone, california. *Journal of Geophysical Research: Solid Earth*, *95*(B7), 11213–11223.
Klimentos, T. (1991). The effects of porosity-permeability-clay content on the velocity of compressional waves. *Geophysics*, *56*(12), 1930–1939.
Lihou, J. C., & Allen, P. A. (1996). Importance of inherited rift margin structures in the early North Alpine Foreland Basin. *Switzerland Basin Research*, *8*(4), 425–442.
Loup, B. (1992). Mesozoic subsidence and stretching models of the lithosphere in Switzerland (Jura, Swiss Plateau and Helvetic realm). *Eclogae Geologicae Helvetiae*, *85*(3), 541–572.
Makhloufi, Y., Rusillon, E., Brentini, M., Moscariello, A., Meyer, M., & Samankassou, E. (2018). Dolomitization of the Upper Jurassic carbonate rocks in the Geneva Basin, Switzerland and France. *Swiss Journal of Geosciences*, *111*, 1–26.
Marti, J. (1969). Rapport de fin de sondage d'Humilly 2.
Matte, P. (2001). The Variscan collage and orogeny (480–290 Ma) and the tectonic definition of the Armorica microplate: A review. *Terra nova*, *13*(2), 122–128.
McCann, T., Pascal, C., Timmerman, M., Krzywiec, P., López-Gómez, J., Wetzel, L., et al. (2006). Post-Variscan (end Carboniferous-Early Permian) basin evolution in western and central Europe. *Geological Society, London, Memoirs*, *32*(1), 355–388.
McSkimin, H., Andreatch, P, Jr., & Thurston, R. (1965). Elastic Moduli of Quartz versus Hydrostatic Pressure at 25 and - 195.8° C. *Journal of Applied Physics*, *36*(5), 1624–1632.
Meyer, M. (2000). *Le complexe récifal kimméridgien-tithonien du Jura méridional interne (France), évolution multifactorielle, stratigraphique et tectonique* (vol. 24). Section des Sciences de la Terre. Université de Genève.
Mondol, N. H., Jahren, J., Bjørlykke, K., & Brevik, I. (2008). Elastic properties of clay minerals. *The Leading Edge*, *27*(6), 758–770.
Moscariello, A. (2016). Geothermal exploration in SW Switzerland. In *Proceeding of the European Geothermal Congress 2016, Strasbourg, France*, pp. 9.
Moscariello, A. (2019). Exploring for geo-energy resources in the Geneva Basin (Western Switzerland): Opportunities and challenges. *Swiss Bulletin für angewandte Geologie*, *24*(2), 105–124.
Müller, W. H., & Briegel, U. (1977). Experimentelle untersuchungen an Anhydrit aus der Schweiz. *Eclogae Geologica Helvetiae*, *70*, 685–699.
Nanda, N. C. (2016). *Seismic data interpretation and evaluation for hydrocarbon exploration and production: a guide for beginners*. Berlin: Springer.
Nur, A., & Simmons, G. (1969). The effect of viscosity of a fluid phase on velocity in low porosity rocks. *Earth and Planetary Science Letters*, *7*(2), 99–108.
Peselnick, L., & Robie, R. A. (1962). Elastic constants of calcite. *Journal of Applied Physics*, *33*(9), 2889–2892.
Pfiffner, O.-A. (1986). *Evolution of the North Alpine foreland basin in the Central Alps*, vol. 8 of *Foreland Basins, Special Publications—International Association of Sedimentologists*. Wiley.
Rafavich, F., Kendall, C. S. C., & Todd, T. (1984). The relationship between acoustic properties and the petrographic character of carbonate rocks. *Geophysics*, *49*(10), 1622–1636.
Rusillon, E. (2018). *Characterisation and rock typing of deep geothermal reservoirs in the greater Geneva Basin*. Earth Science Department: Thesis.
Schegg, R., Cornford, C., & Leu, W. (1999). Migration and accumulation of hydrocarbons in the Swiss Molasse Basin: Implications of a 2D basin modeling study. *Marine and Petroleum Geology*, *16*(6), 511–531.
Schegg, R., & Leu, W. (1996). Clay mineral diagenesis and thermal history of the Thonex well, western Swiss Molasse basin. *Clays and Clay Minerals*, *44*(5), 693–705.
Schilt, S., Oliver, J., Brown, L., Kaufman, S., Albaugh, D., Brewer, J., et al. (1979). The heterogeneity of the continental crust: Results from deep crustal seismic reflection profiling using the Vibroseis technique. *Reviews of Geophysics*, *17*(2), 354–368.
Schwerdtner, W., Tou, J.-M., & Hertz, P. (1965). Elastic properties of single crystals of anhydrite. *Canadian Journal of Earth Sciences*, *2*(6), 673–683.
Sheriff, R. E., & Geldart, L. P. (1995). *Exploration seismology* (2nd ed.). Cambridge: Cambridge University Press.
Signer, C., & Gorin, G. E. (1995). New geological observations between the Jura and the Alps in the Geneva area, as derived from reflection seismic data. *Eclogae Geologicae Helvetiae*, *88*(2), 235–265.
Simmons, G. (1965). Single crystal elastic constants and calculated aggregate properties. Report, Southern Methodist University Press Dallas Texas.
Sommaruga, A., Eichenberger, U., & Marillier, F. (2012). Seismic Atlas of the Swiss Molasse Basin. Edited by the Swiss Geophysical Commission. Matér. Géol. Suisse, Géophys. 44.
Sommaruga, A., Mosar, J., Schori, M., & Gruber, M. (2017). The role of the Triassic evaporites underneath the North Alpine Foreland. *Permo-Triassic Salt Provinces of Europe, North Africa and the Atlantic Margins* (pp. 447–466). New York: Elsevier.
Strasser, A. (1994). Milankovitch cyclicity and high-resolution sequence stratigraphy in lagoonal-peritidal carbonates (Upper Tithonian–Lower Berriasian, French Jura Mountains). In *Orbital forcing and cyclic sequences*, vol. 19, Spec. Publ. Int. Ass. Sediment, pp. 285–301.
Taylor, J. R. (1997). *An introduction to error analysis: the study of uncertainties in physical measurements Error analysis* (2nd ed.). Sausalito: University Science Books.
Thomsen, L. (1986). Weak Elastic-Anisotropy. *Geophysics*, *51*(10), 1954–1966.
Thury, M., Gautschi, A., Mueller, W., Vomvoris, S., Mazurek, M., Naef, H., Pearson, F., & Wilson, W. (1994). Geology and hydrogeology of the crystalline basement of Northern Switzerland. Synthesis of regional investigations 1981-1993 within the Nagra radioactive waste disposal programme. Report, Nationale Genossenschaft für die Lagerung Radioaktiver Abfälle (NAGRA).

Toksöz, M. N., Cheng, C. H., & Timur, A. (1976). Velocities of seismic waves in porous rocks. *Geophysics*, *41*(4), 621–645.
Tosaya, C. A. (1983). *Acoustical properties of clay-bearing rocks*. Department of Geophysics: Thesis.
Valcke, S. L. A., Casey, M., Lloyd, G. E., Kendall, J. M., & Fisher, Q. J. (2006). Lattice preferred orientation and seismic anisotropy in sedimentary rocks. *Geophysical Journal International*, *166*(2), 652–666.
Véron, J. (2005). The Alpine Molasse Basin—review of petroleum geology and remaining potential. *Bulletin für Angewandte Geologie*, *10*(1), 75–86.
Warner, M. (1990). Absolute reflection coefficients from deep Seismic reflections. *Tectonophysics*, *173*(1–4), 15–23.
Wenning, Q. C., Almqvist, B. S. G., Hedin, P., & Zappone, A. (2016). Seismic anisotropy in mid to lower orogenic crust: Insights from laboratory measurements of Vp and Vs in drill core from central Scandinavian Caledonides. *Tectonophysics*, *692*, 14–28.
Wepfer, W., & Christensen, N. (1991). A seismic velocity-confining pressure relation, with applications. *International Journal of Rock Mechanics and Mining Sciences & Geomechanics Abstracts*, *28*(5), 451–456.
Whitney, D. L., & Evans, B. W. (2010). Abbreviations for names of rock-forming minerals. *American mineralogist*, *95*(1), 185–187.
Wilson, M., Neumann, E.-R., Davies, G. R., Timmerman, M. J., Heeremans, M., & Larsen, B. T. (2004). Permo-Carboniferous magmatism and rifting in Europe: introduction. *Geological Society, London, Special Publications*, *223*(1), 1–10.
Woeber, A., Katz, S., & Ahrens, T. (1963). Elasticity of selected rocks and minerals. *Geophysics*, *28*(4), 658–663.
Yan, F. Y., Han, D. H., Yao, Q. L., & Chen, X. L. (2016). Seismic velocities of halite salt: Anisotropy, heterogeneity, dispersion, temperature, and pressure effects. *Geophysics*, *81*(4), D293–E301.
Zappone, A., Fernandez, M., Garcia-Duenas, V., & Burlini, L. (2000). Laboratory measurements of seismic P-wave velocities on rocks from the Betic chain (southern Iberian Peninsula). *Tectonophysics*, *317*(3–4), 259–272.

Publisher's Note